

## Article

# Differential Development Mechanisms of Pore Types under the Sequence Stratigraphic Constraints of the Wufeng–Longmaxi Formation Shale from the Upper Yangtze Platform

Xinlei Wang <sup>1</sup>, Zhaodong Xi <sup>1,\*</sup>, Zhifeng Yan <sup>2,\*</sup>, Songhang Zhang <sup>1</sup>, Shuheng Tang <sup>1</sup> and Donglin Lin <sup>1</sup>

<sup>1</sup> School of Energy Resource, China University of Geosciences, Beijing 100083, China; wangxinlei@email.cugb.edu.cn (X.W.); zhangsh@cugb.edu.cn (S.Z.); tangsh@cugb.edu.cn (S.T.); 3006220022@email.cugb.edu.cn (D.L.)

<sup>2</sup> Liaoning Key Laboratory of Green Development of Mineral Resources, Liaoning Technical University, Fuxin 123032, China

\* Correspondence: xizhaod@cugb.edu.cn (Z.X.); yanzhifeng@lntu.edu.cn (Z.Y.)

**Abstract:** Various types of pores, including organic and inorganic variations, exhibit distinct impacts on the storage capacity of shale gas reservoirs and play a significant role in shale gas occurrence. However, there is a limited number of studies that have quantitatively addressed the developmental characteristics of these diverse pore types and their primary controlling factors. This paper explores the development of inorganic pores, specifically interparticle pores and intraparticle pores, as well as organic matter (OM) pores within the shales of the Wufeng–Longmaxi Formation in the Upper Yangtze region. Parameters such as areal porosity, pore diameter, and pore number based on the FE-SEM and image digitization are discussed. Additionally, the influence of the sedimentary environment on the development of various pore types through integrated wavelet transform techniques and geochemical analysis are analyzed. This analysis reveals the distinctive mechanisms governing the development of pore types under the sequence stratigraphic constraints. The findings reveal that the Wufeng–Longmaxi Formation within the study area can be classified into four systems tracts (transgressive systems tracts TST1 and TST2, and highstand systems tracts HST1 and HST2). Within TST1+HST1, OM pores emerge as the predominant pore type, contributing to over 65% of the porosity. TST2 similarly displays OM pores as the dominant type, comprising over 45% of the total porosity, with an average OM areal porosity of 7.3%, notably lower than that of TST1+HST1 (12.7%). Differences in OM pore development between TST1+HST1 and TST2 shales are attributed to variations in OM abundance and type. In HST2, inorganic pores are the dominant pore type, primarily consisting of interparticle pores associated with clay minerals, contributing to more than 50% of the porosity, while OM pores remain almost undeveloped. The frequent sea level fluctuations during the sequence stratigraphic evolution caused variations in sedimentary environments across different depositional sequences. These differing depositional environments lead to varying OM content and types, mineral genesis, and content, ultimately resulting in disparities in the development of shale pore types within different sequences.

**Keywords:** shale; pore types; sequence stratigraphy; sedimentary environment; organic matter



**Citation:** Wang, X.; Xi, Z.; Yan, Z.; Zhang, S.; Tang, S.; Lin, D. Differential Development Mechanisms of Pore Types under the Sequence Stratigraphic Constraints of the Wufeng–Longmaxi Formation Shale from the Upper Yangtze Platform. *Processes* **2023**, *11*, 3436. <https://doi.org/10.3390/pr11123436>

Academic Editor: Carlos Sierra Fernández

Received: 20 November 2023

Revised: 5 December 2023

Accepted: 12 December 2023

Published: 15 December 2023



**Copyright:** © 2023 by the authors. Licensee MDPI, Basel, Switzerland. This article is an open access article distributed under the terms and conditions of the Creative Commons Attribution (CC BY) license (<https://creativecommons.org/licenses/by/4.0/>).

## 1. Introduction

Due to new techniques, particularly hydraulic fracturing and advances in horizontal drilling, the extraction of oil and gas from shale has become economically viable [1,2]. Shale gas reservoirs differ from conventional reservoirs in that they consist of a heterogeneous porous medium characterized by intricate pore sizes and various pore types, which add intricacies to gas storage and conversion mechanisms [3–5]. This complexity arises because different pore types have varying effects on the storage capacity of shale gas reservoirs and influence the occurrence of shale gas [6–8]. Therefore, conducting quantitative research on

the developmental characteristics and primary controlling factors of these distinct pore types holds significant importance for characterizing shale reservoirs and advancing shale gas exploration and development.

The precise characterization of the pore size of shale gas reservoirs and the factors governing it have garnered substantial research attention over the past decade, with a primary focus on controlling factors [9–17]. However, systematic research based on pore types and their control factors remains limited. Pore types in shale can be classified and analyzed based on the morphology of adsorption and desorption curves obtained from low-temperature N<sub>2</sub> adsorption (LTN<sub>2</sub>A) and the morphology of injection and ejection curves from mercury intrusion porosimetry (MIP) [18–20]. Furthermore, direct observations can be made through experimental techniques such as scanning electron microscopy (SEM) [10]. Significant differences exist between the pore types (e.g., slit-shaped pores, wedge-shaped pores) identified through hysteresis loop analysis and the actual pore morphology, which cannot be quantitatively characterized. Currently, the primary method for studying shale pore types involves SEM combined with digital image processing. Using classification schemes such as that previously proposed [10], researchers categorize these pores into interparticle pores, intraparticle pores, and organic matter (OM) pores for in-depth analysis. Image analysis effectively utilizes high-resolution SEM images to determine various properties of different pore types, including their number, size, geometric shape, and area [21–24].

The mineral content and genesis, as well as the OM content and type, can significantly influence the prevalence of different pore types within shale [11,12,14,25]. Shale enriched in OM typically develops a substantial quantity of OM pores [26]. The type of OM plays a crucial role in controlling the development of these OM pores. In the case of the Wufeng–Longmaxi Formation shale, OM pores are more prevalent within pyrobitumen and less so in other macerals, such as graptolites [27,28]. The mineral matrix pores within the Wufeng–Longmaxi Formation shale primarily consist of interparticle pores. These interparticle pores typically develop at the interfaces between brittle minerals such as quartz, carbonate minerals, and pyrite, and can be found between clay mineral particles such as illite, kaolinite, and chlorite [29–31]. Generally, shales with a high content of brittle minerals exhibit greater resistance to compaction, making them more likely to retain their primary interparticle pores compared to shales rich in clay minerals [32]. Recent research has revealed that biogenic quartz plays a dual role in shale characteristics. It not only contributes to shale brittleness but also forms a rigid framework that can preserve the primary pores of shale. Furthermore, it influences the distribution of OM and the development of OM pores [33–36]. Additionally, intraparticle dissolution pores develop in carbonate minerals and feldspar. Studies suggest that these dissolution pores result from the dissolution of chemically unstable minerals during burial diagenesis [7,10].

As the mineral composition and OM content within the formation change, the porosity and dominant pore types of shale also undergo modification [15]. This stratigraphic variability may be linked to the process of sedimentation and diagenesis [37], and it is further impacted by fluctuations in relative sea levels during the evolution of sequence stratigraphy [38,39]. A multitude of previous studies have illustrated the role of sequence stratigraphy in shaping the enrichment of OM in shale [40–45]. Notably, OM tends to be most abundant in the transgressive systems tract (TST) or in proximity to the maximum flooding surface (MFS), with the highest total organic carbon (TOC) value serving as a marker for the MFS [46]. However, there has been insufficient focus on investigating the variations in shale pore type characteristics within the context of sequence stratigraphy, and the understanding of the mechanisms influencing these variations remains limited.

The focus of the present investigation lies on the marine shale of the Wufeng–Longmaxi Formation situated in northern Guizhou of South China's upper Yangtze Platform. Various pore types were systematically identified and quantitatively characterized using SEM and image analysis. The emphasis is on leveraging the enrichment patterns of major and trace elements to reconstruct the redox conditions and paleoproductivity during the sedimen-

tation of the Wufeng–Longmaxi Formation shale. Furthermore, an analysis is conducted to explore the impact of the sedimentary environment on both the enrichment of OM and the mineralogical composition of the shale. The findings of this study are subsequently integrated into a sequence stratigraphic framework, allowing for an analysis of the distinct development mechanisms of shale pore types within the context of sequence stratigraphy.

## 2. Geological Setting

Since the Ordovician, the Yangtze Platform has undergone multiple tectonic movements, giving rise to a series of paleo-uplifts in the vicinity of the Sichuan Basin. These uplifts notably include the Chuanzhong Uplift, the Xuefeng Uplift, and the Qianzhong Uplift, collectively contributing to the establishment of a relatively low-lying tectonic framework within the Sichuan Basin and its surrounding regions [47]. In response to two significant global transgressions during the late Ordovician and Early Silurian, the sea level increased rapidly, culminating in the formation of a low energy and anoxic sedimentary environment. This period witnessed the deposition of a thick layer of OM-rich shale, with prominent examples being the upper Ordovician Wufeng Formation and the lower Silurian Longmaxi Formation.

Well YC1 is positioned in the northern part of the Guizhou Province in southern China. It is situated along the southwestern edge of the Yangtze Platform and is adjacent to the Sichuan Basin (Figure 1A,B). The burial depth of the Wufeng Formation in well YC1 ranges from 2030.31 to 2037.38 m. The lithology of this formation primarily consists of grey black silty shale and black carbonaceous shale, both exhibiting a high OM content (TOC > 2%) (Figure 1C). Meanwhile, the burial depth of the Longmaxi Formation in well YC1 ranges from 1854.96 to 2030.31 m. The lithological composition of the Longmaxi Formation mainly comprises grey black shale and grey black silty shale, characterized by a low OM content (TOC < 2%). The described variations of lithology and TOC content are comparable to the Wufeng–Longmaxi Formation shales elsewhere in the Upper Yangtze Platform and correlative “hot shales” elsewhere in the world [48,49].

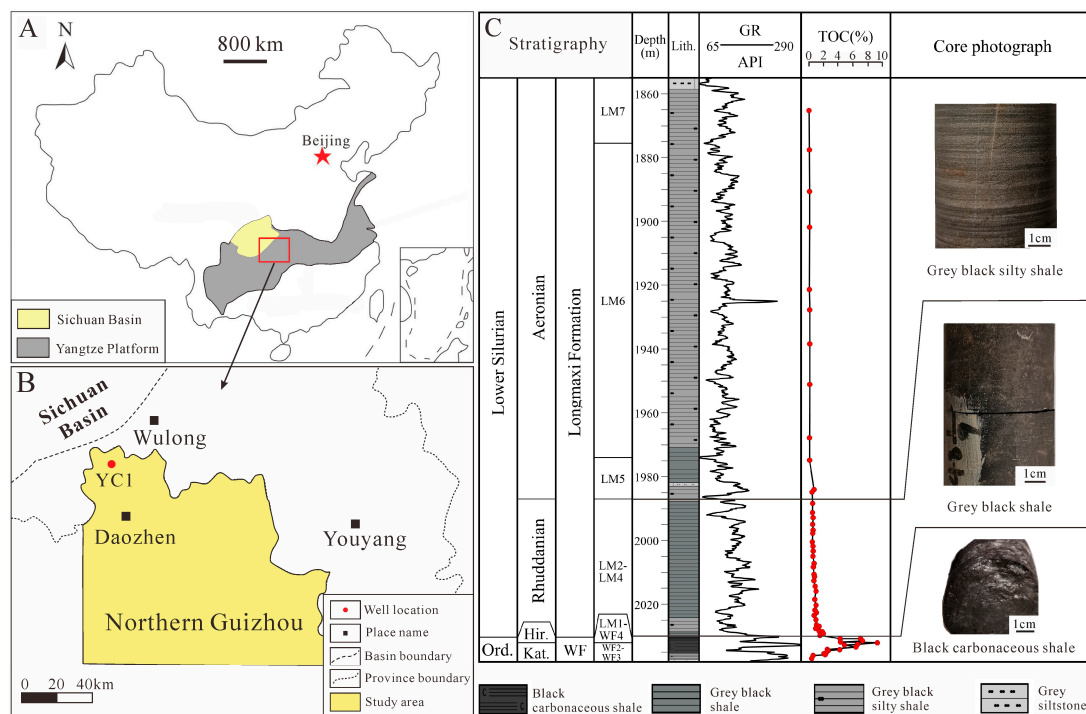


**Figure 1.** (A) Location of the study area (modified from [50]). (B) Location of the sampling YC1 well (modified from [50]). (C) Stratigraphic column, TOC, and core photographs of the Wufeng–Longmaxi Formation in YC1 well. Ord. = Ordovician, WF = Wufeng Formation, Kat. = Katian, Hir. = Hirnantian, Lith. = Lithology.

### 3. Experimental Methods and Data Processing

#### 3.1. Sampling and Methodology

A total of 52 fresh core samples were systematically collected from the Wufeng–Longmaxi Formation shale in well YC1, situated in the northern part of Guizhou. Each of these samples underwent comprehensive analysis, encompassing determinations of total organic carbon (TOC) content as well as major and trace element concentrations. Moreover, a subset of 21 samples was subjected to a more detailed assessment using X-ray diffraction (XRD) [51], scanning electron microscopy-cathodoluminescence (SEM-CL), and helium porosimeter. The methodologies employed throughout this study mirror those applied in our previous studies, with a detailed description being included in these references [52,53].

#### 3.2. Processing FE-SEM Image Data

High-resolution SEM images at the nanoscale were subjected to image analysis using Image Pro Plus (IPP) software. The SEM images were first binarized using manual thresholding (Figure 2). Threshold methods segment greyscale images into features of interest and background using lower and upper greyscale difference threshold values [54]. Pores can be described as an area where the greyscale is lower than a threshold, because the area of pores is invariably lower than other distinct areas of the image [54]. Different types of pore information, including pore area, diameter, and quantity, were extracted through spatial calibration and count/size. The method of Artificial Identification of Area of Interests (AOI) is used to extract pore structure information from OM and major minerals in shale, as shown in Figure 2. It is worth noting that due to the limited magnification of SEM, pores smaller than 8 nm cannot be identified, and most of these pores should be OM pores.

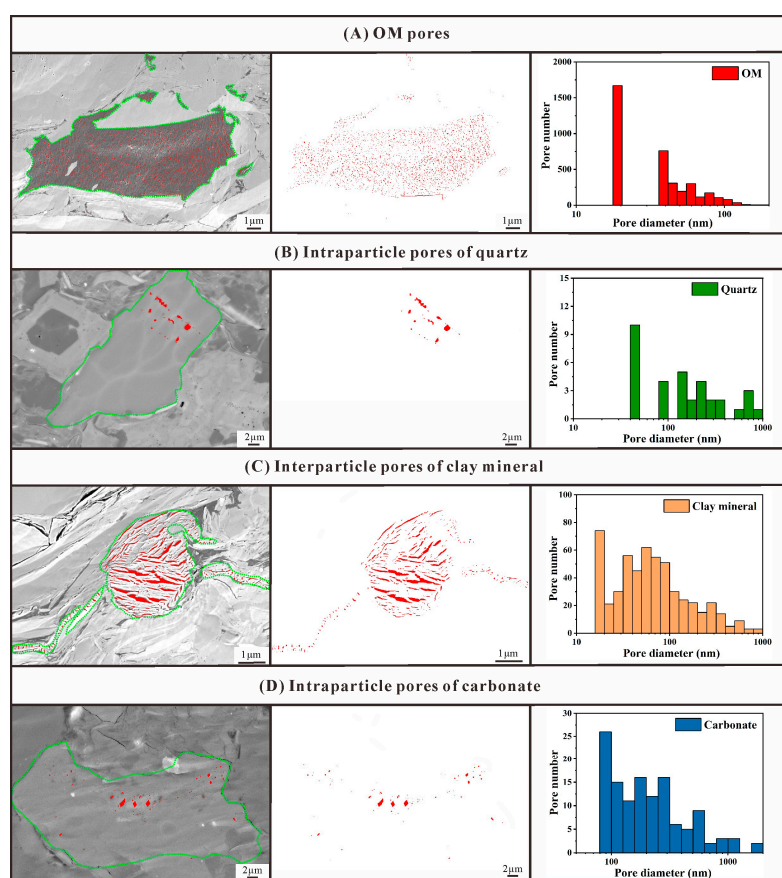


**Figure 2.** Image analysis of different pore types using IPP6.0 software. (A) The extraction of OM pores from OM. (B) The extraction of intraparticle pores from quartz. (C) The extraction of interparticle pores from clay mineral. (D) The extraction of intraparticle pores from carbonate mineral.

### 3.3. Data Processing of Major and Trace Elements and Its Geological Significance

The concentration and enrichment characteristics of Mo and U are commonly applied for the reconstruction of redox environments. In oxic aqueous systems, Mo predominantly exists in the form of molybdate ( $\text{MoO}_4^{2-}$ ) [55,56]. However, in anoxic or euxinic (anoxic-sulfidic) aqueous systems, molybdate ( $\text{MoO}_4^{2-}$ ) transforms into thiomolybdate ( $\text{MoO}_{4-x}\text{S}_x^{2-}$ ) or Mo polysulfide. These compounds can be sequestered by OM or iron sulfide, leading to their precipitation and consequent Mo enrichment in sediments. As a result, strong Mo enrichment serves as an indicative marker of a sulfidic environment. In oxic marine settings, U predominantly exists in the form of  $\text{U}^{6+}$  as  $\text{UO}_2(\text{CO}_3)_3^{4-}$ . However, under anoxic conditions, soluble  $\text{U}^{6+}$  can be reduced to  $\text{U}^{4+}$ , a form that is generally insoluble and readily adsorbed by sediments [55]. Thus, the substantial U enrichment is a significant indicator of an anoxic environment. To measure the extent of Mo and U enrichment, the enrichment factor (EF) is employed, offering insight into the relative enrichment or depletion of an element in relation to the Post-Archean Australian shale (PAAS).  $X_{\text{EF}}$  can be obtained using the following equation:

$$X_{\text{EF}} = (X/\text{Al})_{\text{sample}} / (X/\text{Al})_{\text{PAAS}} \quad (1)$$

where  $X$  and  $\text{Al}$  represent the concentrations of a specific element and  $\text{Al}$  in the shale sample. The trace element and  $\text{Al}$  concentration data for the PAAS are provided in McLennan [57].

In the modern ocean, a Mo concentration exceeding 100 ppm indicates a consistently euxinic environment characterized by a substantial presence of aqueous Mo. A concentration ranging from 25 ppm to 100 ppm reflects a persistent anoxic environment, while a concentration between 2 ppm and 25 ppm signifies predominantly oxic conditions [58].

In oxic aqueous systems, Cu, Ni, and Zn predominantly exist as organometallic complexes, with a minor portion occurring as soluble ions [59]. The strong enrichment of Cu, Ni, and Zn is indicative of a substantial influx of OM into the sediment. Under oxic conditions, OM degrades, subsequently releasing Cu, Ni, and Zn back into the water. These elements then combine with sulfur (S) to form insoluble sulfide compounds, which under reducing conditions, particularly sulfate-reducing conditions, are integrated into pyrite as solid solutions [55]. Therefore, the concentrations of Cu, Ni, and Zn serve as reliable indicators of paleoproductivity. The origins of elements within sediments primarily encompass terrigenous, biogenic, and hydrothermal sources. When estimating paleoproductivity using geochemical elements, it is essential to consider only biogenic elements for productivity assessments, as they contribute to paleoproductivity inversion [60]. Consequently, the influences of terrigenous and hydrothermal origins must be eliminated. Given the limited impact of formation of thermal fluid input within the study area, the contribution from hydrothermal sources can be disregarded. To mitigate the influence of terrigenous origins on the trace element content, trace element values in the samples were subjected to correction. The formula for this correction is as follows:

$$X_{\text{XS}} = X_{\text{sample}} - \text{Ti}_{\text{sample}} \times (X/\text{Ti})_{\text{PAAS}} \quad (2)$$

where  $X_{\text{sample}}$  and  $\text{Ti}_{\text{sample}}$  represent the concentrations of a specific element and  $\text{Ti}$  in the shale sample, respectively. The trace element and  $\text{Ti}$  concentration data for PAAS are provided in McLennan [57].

$\text{Si}_{\text{ex}}$  denotes Si that is not associated with terrigenous minerals in rocks. It is determined by subtracting the Si content linked to terrigenous clastic Al from the total Si content of the rock [61]. The calculation for  $\text{Si}_{\text{ex}}$  can be performed using the following equation:

$$\text{Si}_{\text{ex}} = \text{Si}_{\text{sample}} - (\text{Si}/\text{Al})_{\text{PAAS}} \times \text{Al}_{\text{sample}} \quad (3)$$

where  $(\text{Si}/\text{Al})_{\text{PAAS}}$  is calculated based on PAAS, which has a value equal to 3.11 [62,63].

## 4. Results

### 4.1. Sequence Stratigraphic Division Based on Wavelet Analysis

At present, logging data represent the geological information characterized by the highest attainable resolution and optimal continuity. This data type contains an extensive repository of sedimentary cycle details within the strata, rendering it an ideal candidate for the quantitative division of sequence stratigraphy [64]. By employing wavelet analysis, it becomes possible to amplify the geological characteristics inherent in high-resolution logging signals, operating in the two-dimensional time-frequency domain. This analytical method also serves to process one-dimensional logging signals, thus accentuating their underlying geological characteristics [65]. Consequently, through continuous wavelet transform processing, logging curves can be dissected. These curves, formed through the superposition of multiple sedimentary cycles bearing distinct periods, are disentangled into independent periodic cycles, each exhibited through a scale (a) [64,66]. The magnitude of the scale (a) parameter inversely correlates with the frequency of the wavelet curve, impacting its resolution. Larger values of scale (a) correspond to wavelet curves with lower frequency and reduced resolution, indicative of the long-period component within the logging signal. This, in turn, signifies the presence of extended sedimentary cycles and substantial formation thickness, facilitating the differentiation of long-term cycles [66]. Conversely, smaller scale (a) values correlate with higher frequency wavelet curves, yielding higher resolutions. Such characteristics denote the short period component within the logging signal, highlighting the presence of condensed sedimentary cycles and comparatively modest formation thickness, thereby delineating medium and short-term cycles [66]. Previous studies have convincingly demonstrated that the temporal boundaries of long-term, medium-term, and short-term cycles within the strata closely align with those of the third-, fourth-, and fifth-order sequences (Table 1) [67].

**Table 1.** Orders and driving mechanism of sequence cycles [68].

Sequence Stratigraphic Term	Deposition Cycles	Time Range (Ma)	Genetic Mechanism	
First-order megasequence		200–400	Stereotype sea level changes caused by the movement of tectonic plates	Global sea level changes caused by Pangaea formation and breakup
Second-order supersequence		10–40		Global sea level changes caused by ocean ridge spreading system
Third-order sequence	long-term cycle	1–10		Global sea level changes caused by the variation in mid-ocean ridge and the oscillation of continental glacier + regional sea level changes influenced by intraplate tectonic subsidence and uplift
Fourth-order subsequence sets or system tract	medium-term cycle	0.4	Glacier type sea-level changes caused by	Long eccentricity cycle
Fifth-order subsequence	short-term cycle	0.1	Milankovitch	Short eccentricity cycle
Sixth-order cyclothem		0.02–0.04	astronomical cycle	Precession and obliquity cycle
Seventh-order alternating laminae		0.002–0.005	Long eccentricity cycle	Change of glacier and geoid

The natural gamma curve (GR) of well YC1 within the study area has undergone wavelet analysis. Figure 3 depicts the resultant wavelet scalogram derived from the wavelet transformation, where blue–green hues indicate lower values, and yellow–red hues signify higher values. Observing the wavelet scalogram, it becomes apparent that a distinct two-stage color transition at the scale  $a = 250$  is predominantly indicative of substantial, large-scale sedimentary cycles. This feature proves valuable in demarcating

long-term cycles (Figure 3). Additionally, a noticeable cyclic shift emerges at the scale  $a = 120$ , offering a useful criterion for segmenting medium-term cycles (Figure 3). Based on the characteristics observed in the change curve of the wavelet coefficient at scale  $a = 250$ , along with the corresponding color transition in the wavelet scalogram, two distinct third-order sequences were discerned within the Wufeng–Longmaxi Formation in well YC1. Expanding further, the characteristics exhibited in the change curve of the wavelet coefficient at scale  $a = 120$ , alongside the associated color shift in the wavelet scalogram, facilitated the identification of the transgressive systems tract (TST) and highstand systems tract (HST) contained within the third-order sequence (Figure 3). Furthermore, a robust alignment is noted between lithological characteristics, logging curve features, and each sequence boundary, rendering them more distinct and discernible within the GR and SP curves.

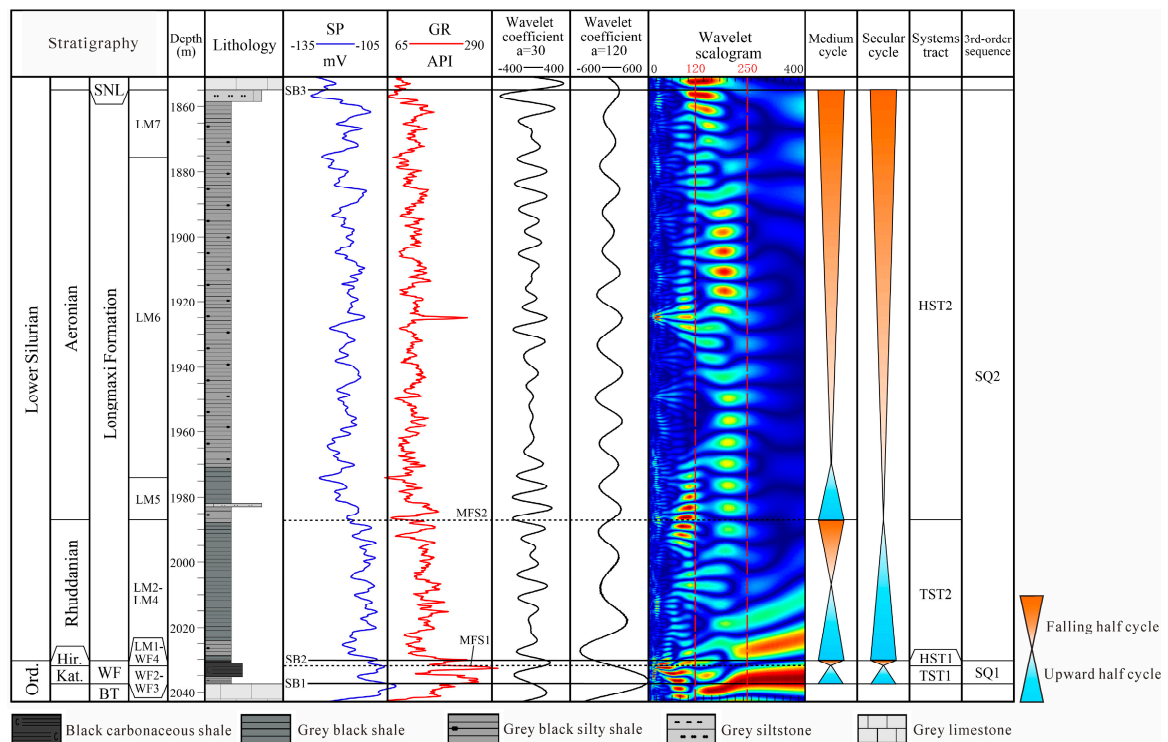


**Figure 3.** Stratigraphic framework construction of the Wufeng–Longmaxi Formation in well YC1. Ord. = Ordovician, BT = Baota Formation, WF = Wufeng Formation, SNL = Shiniulan Formation, Kat. = Katian, Hir. = Hirnantian, TST = Transgressive systems tract, HST = Highstand systems tract, SB = Sequence boundary, MFS = Maximum flooding surface.

In summary, the division of the Wufeng–Longmaxi Formation in well YC1 into two distinct third-order sequences, SQ1 and SQ2, is derived from a comprehensive analysis of lithological characteristics, logging curve attributes, wavelet coefficient change curve features, and alterations in the color patterns of the wavelet scalogram. SQ1 corresponds to the Wufeng Formation and encompasses both the TST1 and HST1. On the other hand, SQ2 corresponds to the Longmaxi Formation and comprises the TST2 and HST2 intervals. Notably, the Guanyinqiao bedding forms a significant part of HST1 within the Wufeng Formation [37]. Given its thin nature, making it challenging to identify in the drill core of the study area and having limited sample points, TST1 and HST1 are considered a unified section in the subsequent discussion.

#### 4.2. TOC and Mineralogical Composition

The TOC of shales within TST1 and HST1 varies from 2.04% to 9.24%, averaging 4.70%. The primary minerals within this interval are quartz, carbonate minerals, and clay minerals

(Table 2). Notably, the average quartz content constitutes 34.50%, followed by an average of 38.17% for carbonate minerals, and an average of 15.33% for clay minerals. Moving to TST2, the TOC of shales ranges between 0.50% and 1.98%, with an average value of 0.89%. Correspondingly, the average mineralogical composition within this interval consists of 34.08% quartz, 20.00% carbonate minerals, and 24.48% clay minerals. For HST2, the TOC of shales ranges from 0.05% to 0.73%, averaging 0.20%. The average content of the primary minerals within this interval comprises 27.86% quartz, 31.91% carbonate minerals, and 23.24% clay minerals.

**Table 2.** TOC and mineralogical composition of the Wufeng–Longmaxi Formation shale samples from well YC1.

Shale Components (wt %)	TST1 + HST1			TST2			HST2		
	Min.	Max.	Ave.	Min.	Max.	Ave.	Min.	Max.	Ave.
TOC	2.04	9.24	4.7	0.5	1.98	0.89	0.05	0.73	0.2
quartz	23	53	34.5	22.4	38	34.08	20	31.5	27.86
K-feldspar	0	9	3.83	2.1	12	7.22	2.7	7.7	5.32
albite	4	14	7.83	4.9	20	13.58	9.6	14.3	11.09
calcite	11	53	36.5	13	26	17.52	17.2	46.8	24.76
dolomite	0	6	1.67	0	4	2.48	3.3	10.1	7.15
pyrite	0	1	0.33	0	2.1	0.62	0	2.4	0.57
illite	44	58	49	40	46	43.5	13	36	22.7
mixed-layer illite-smectite	28	40	33.83	38	41	39.75	46	65	55.3
kaolinite	0	0	0	0	0	0	4	7	5.4
chlorite	10	24	17.17	13	19	16.75	14	22	16.6
clay minerals	12	21	15.33	18	41.4	24.48	9.5	27.6	23.24
carbonates	16	53	38.17	13	26	20	26	51.6	31.91

#### 4.3. Pore Types

According to the descriptive classification scheme proposed by Loucks et al. [9,10], pores within the Wufeng–Longmaxi Formation shale are categorized into OM pores, interparticle pores, and intraparticle pores.

##### 4.3.1. OM Pores

In the study area, the OM pores of the Wufeng–Longmaxi Formation shale exhibit predominantly circular and oval morphologies, encompassing pore sizes ranging from several nanometers to hundreds of nanometers (Figure 4A–C). A noticeable correlation exists between the number, porosity, and the broader distribution of pore sizes for OM pores in the shale of the study area and the OM morphology. The OM found in shale samples can be categorized into three categories based on its morphology: gap-filling OM, scattered OM, and striped OM.

(1) Gap-filling OM: Gap-filling OM is predominantly dispersed among authigenic minerals, primarily quartz and pyrite (Figure 5A–C). Previous studies have indicated that OM in the shale of the Wufeng–Longmaxi Formation is mainly composed of pyrobitumen. Oil-prone macerals (such as algae) generate oil and gas, eventually transforming into pyrobitumen during thermal maturation. These pyrobitumens subsequently migrate short distances to occupy primary interparticle pores, leading to the formation of gap-filling OM. This type of OM contains a substantial number of OM pores, with areal porosity ranging from 5.0% to 24.2%, averaging 12.7% (Figure 6A). The pore sizes range from 8 to 100 nm (Figure 7A). As pore size increases, the number of pores gradually decreases, with pores smaller than 20 nm being the most prevalent.

(2) Scattered OM: Scattered OM often appears as irregular blocks (Figure 5D–F), with particle dimensions typically reaching the micrometer level. Scattered OM is the result of local enrichment of pyrobitumen. This type of OM contains a substantial number of OM pores, with areal porosity ranging from 2.8% to 12.8%, averaging 7.3% (Figure 6A). The

pore sizes range from 10 to 100 nm (Figure 7B), with pores smaller than 30 nm being the most developed.

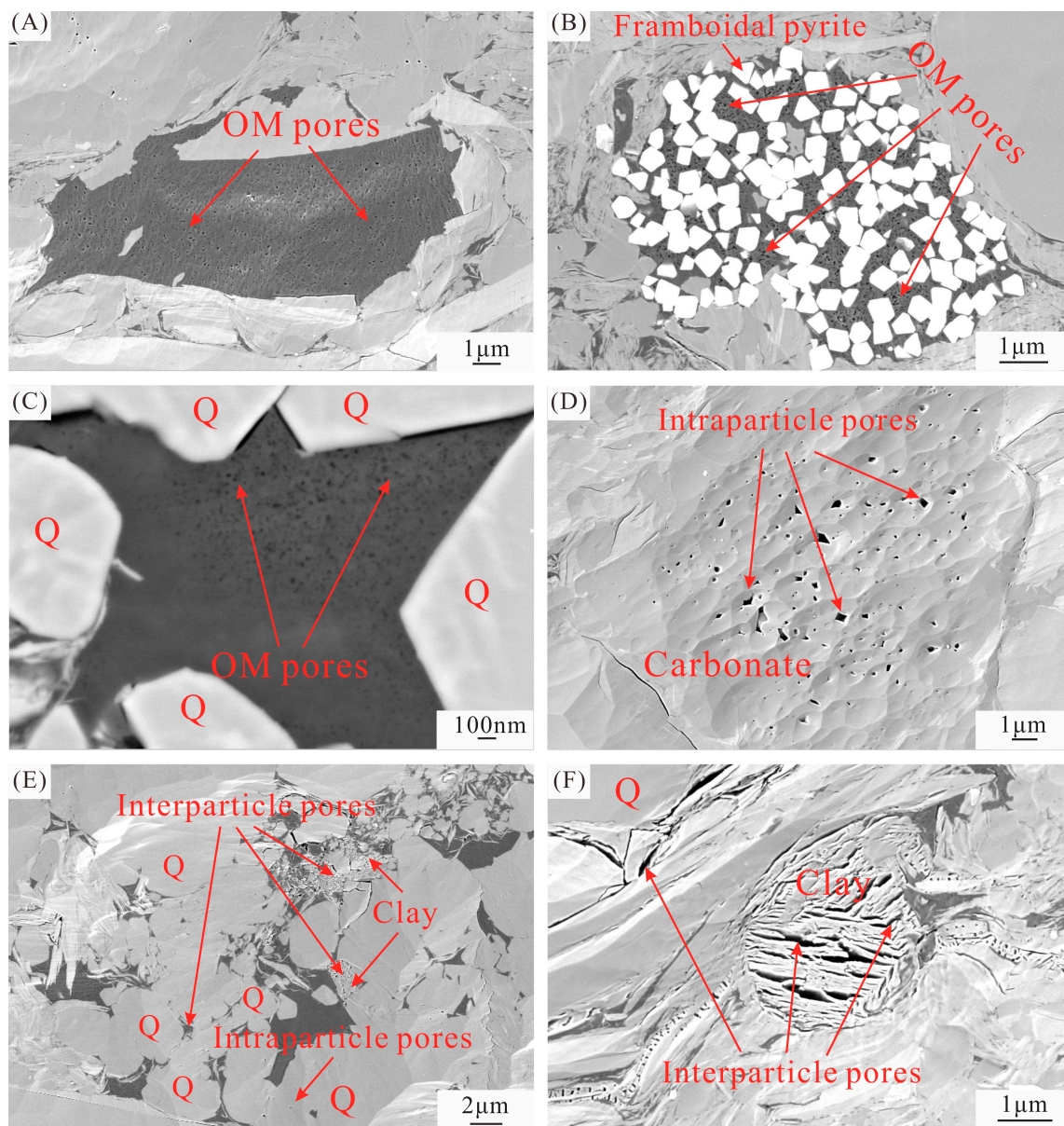


**Figure 4.** SEM images of different types of pores in the Wufeng–Longmaxi Formation shale samples. (A) Abundant OM pores in the TST1 shale samples. (B) OM filling between framboidal pyrite grains, with abundant OM pores, TST1. (C) OM filling between biogenic quartz particles, with abundant OM pores, TST1. (D) Intraparticle pores within carbonate minerals, TST2. (E) Intraparticle pores within detrital quartz grains, and interparticle pores at the contacts of quartz and pyrite grains, TST2. (F) Interparticle pores at the contacts of detrital quartz grains and clay minerals, HST2. OM, organic matter; Q, quartz.

(3) **Striped OM:** Striped OM typically presents an irregular striped distribution within the matrix (Figure 5G–I). Based on its morphological characteristics, it is suggested that this type of OM may be graptolite. This observation aligns with findings by Yang et al. and Delle Piane et al. [69,70], who also noted the absence of developed OM pores in graptolites from the Wufeng–Longmaxi Formation shale, consistent with SEM observations in this study. This type of OM primarily develops shrinkage cracks only at the edges of particles, with areal porosity ranging from 0.0% to 6.4%, averaging 0.9% (Figure 6A).

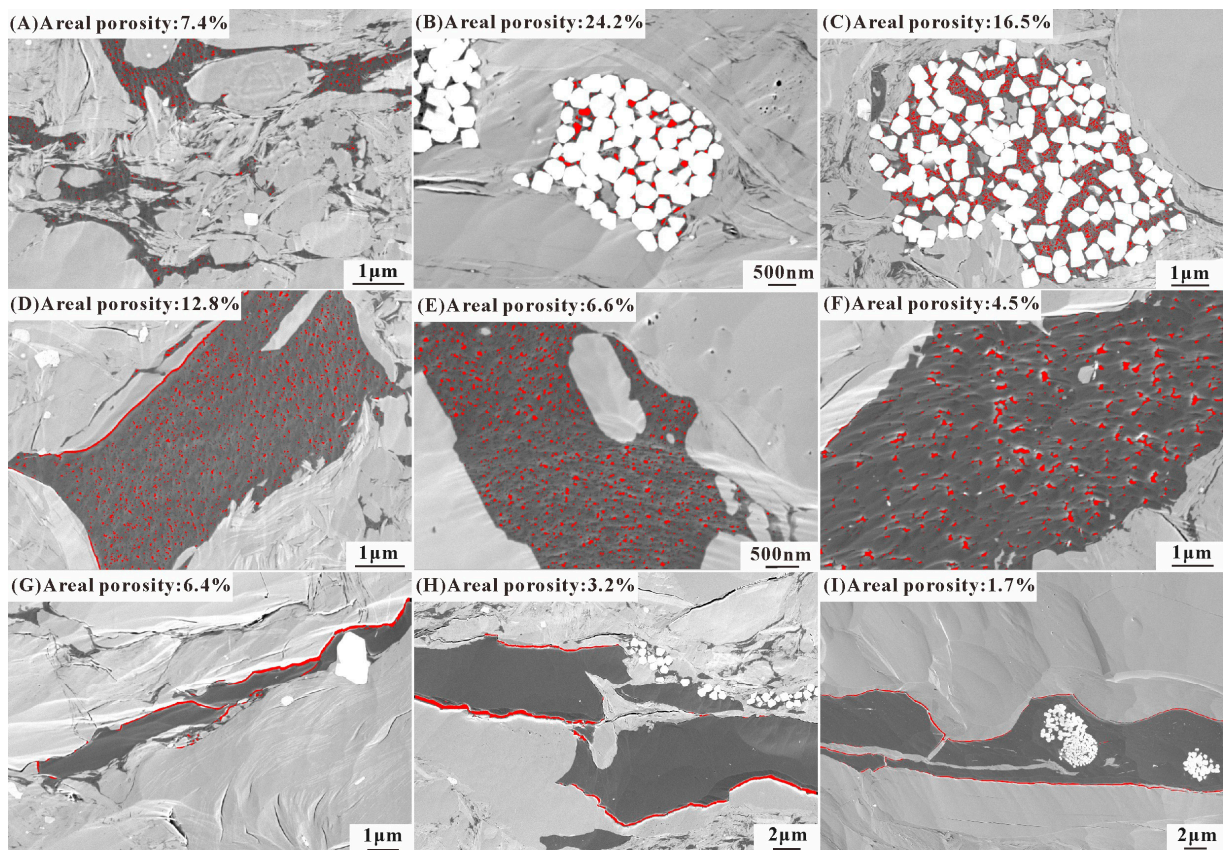


**Figure 5.** SEM images and areal porosity of different OM categories in the Wufeng–Longmaxi Formation samples. (A–C) Gap-filling OM. (D–F) Scattered OM. (G–I) Striped OM.

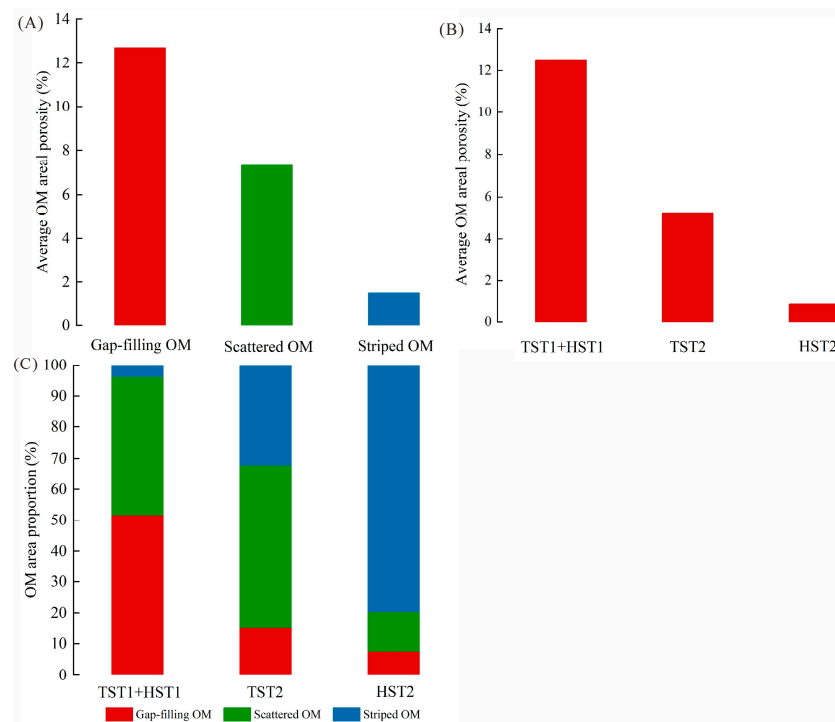


**Figure 6.** (A) Average areal porosity of various OM types. (B) Average OM areal porosity in the Wufeng–Longmaxi Formation shale samples from well YC1. (C) Area proportion of different OM types in the Wufeng–Longmaxi Formation shale samples from well YC1.

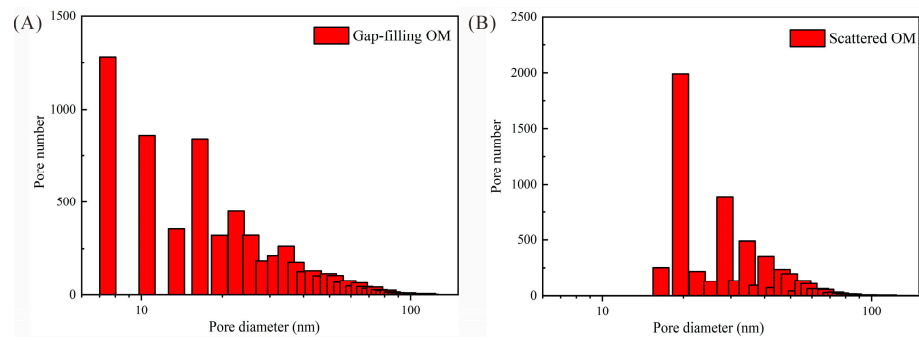


**Figure 7.** Pore diameter distribution of organic pores in different OM categories. (A) Gap-filling OM. (B) Scattered OM.

#### 4.3.2. Inorganic Pores

Interparticle pores often occur between clay minerals, quartz, and pyrite particles (Figure 4E,F). The interparticle pore morphology associated with authigenic minerals, such as authigenic quartz and pyrite, is primarily triangular. Typically, these pores represent the residual primary interparticle pores after strong compaction. Subsequent diagenesis usually results in most of these pores being filled with OM or clay minerals (Figure 4B,C). In contrast, the interparticle pores associated with terrigenous detrital minerals (clay minerals) often appear as narrow slit-shaped openings. Examination of the SEM images of the samples reveals a small number of pores (with diameters between 50–200 nm) that have a widely varying and uneven distribution of interparticle pore sizes (Figure 8).

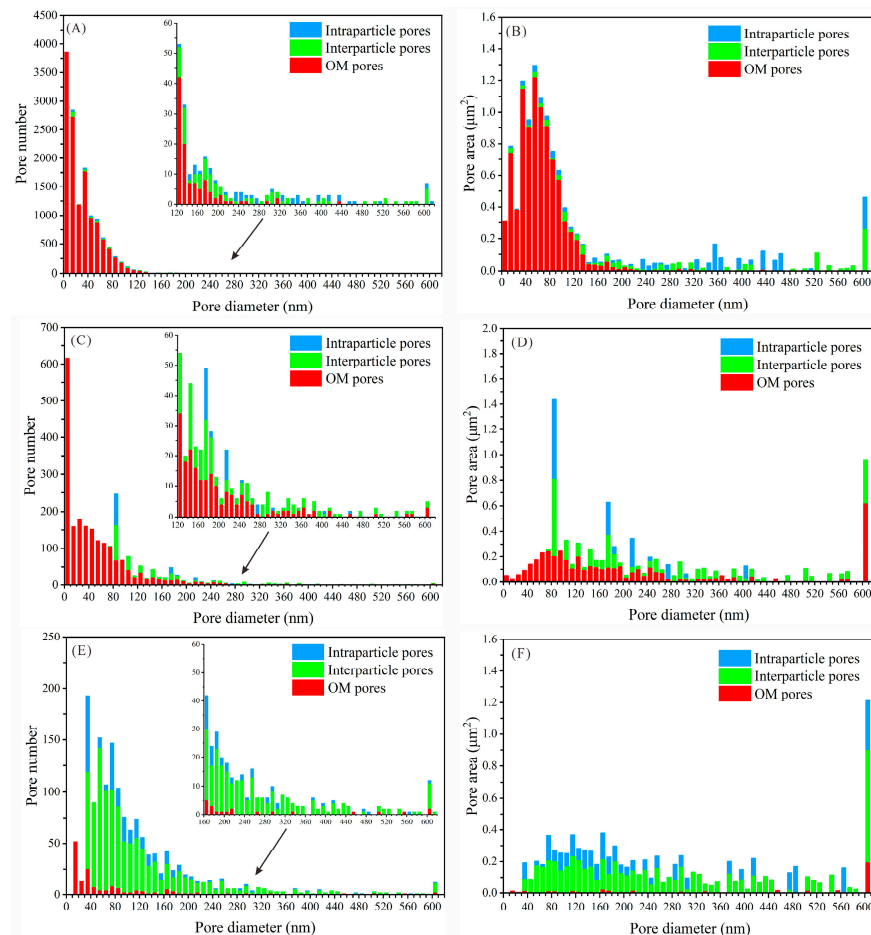


**Figure 8.** Quantity and pore area distribution of various pore types obtained by image analysis. (A,B) are from TST1 + HST1; (C,D) are from TST2; (E,F) are from HST2).

Intraparticle pores are notably prevalent within carbonate and quartz particles (Figure 4D,E). For carbonate minerals, intraparticle pores typically manifest as circular or triangular structures, with pore sizes generally measuring in the hundreds of nanometers or micrometers, likely formed through dissolution processes [71]. Meanwhile, intraparticle pores within quartz particles primarily adopt an isolated circular configuration, characterized by small, disjointed pore sizes. These intraparticle pores might represent fluid inclusions that were unveiled through ion milling [12,34,72]. The number of intraparticle pores is relatively small (with diameters between 50 and 500 nm), resulting in a wide and uneven distribution of pore sizes (Figure 8). Moreover, intraparticle pores are typically larger than interparticle pores, and they are scattered within the mineral particles, resulting in greater spacing and relatively poor connectivity.

#### 4.4. Characteristics of Pore Types under Sequence Stratigraphic Constraints

The TST1 and HST1 shale samples predominantly consist of gap-filling OM and scattered OM (accounting for 90%), with an average OM areal porosity of 12.5% (Figure 6B,C). In this section, OM pores in the shale are the most abundant (with diameters between 8 and 50 nm), contributing the most to the pore area (Figures 8 and 9). The number of intraparticle pores is secondary, primarily dominated by intraparticle pores within carbonate minerals. Interparticle pores are the least numerous, primarily found within clay minerals (Figures 8 and 9). The TST2 shale sample is predominantly composed of scattered OM and striped OM (80%), with an average OM areal porosity of 5.2% (Figure 6B,C). In this section, OM pores in the shale are the most numerous (with diameters between 8 and 50 nm), contributing the most to the pore area (Figures 8 and 9). Interparticle pores are secondary, primarily dominated by interparticle pores within clay minerals, while intraparticle pores are less prevalent, primarily found within carbonate minerals (Figures 8 and 9). The HST2 shale sample mainly consists of striped OM (80%), with an average OM areal porosity of 0.9% (Figure 6B,C). In this section, the number of OM pores in shale samples is relatively small, with a predominant development of interparticle pores (with diameters between 50 and 200 nm), primarily dominated by interparticle pores within clay minerals (Figures 8 and 9). OM pores are the dominant pore type in TST1 and HST1, contributing over 65% to the total porosity. Similarly, OM pores are also the dominant pore type in TST2, contributing over 45% to the total porosity. In HST2, the dominant pore type is interparticle pores in clay minerals, contributing over 50% to the total porosity (Figure 9).

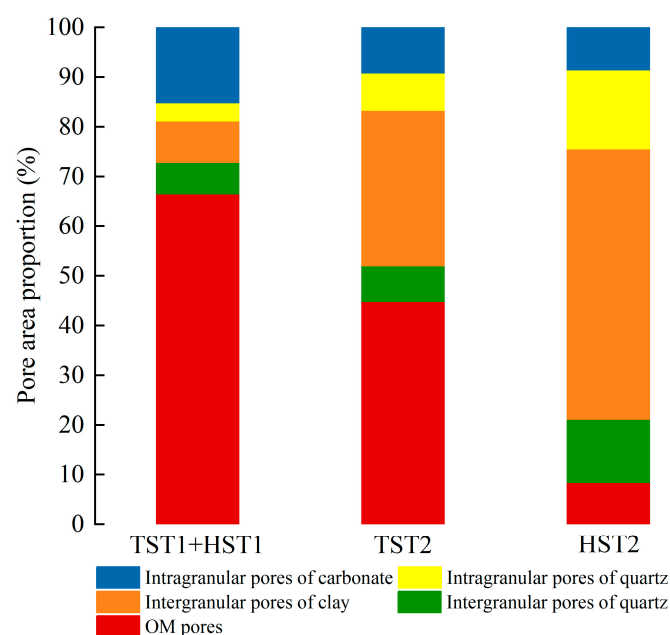


**Figure 9.** The contributions of different pore types in the Wufeng–Longmaxi Formation shale samples.

#### 4.5. Major and Trace Elements

The contents and enrichment factors of Mo and U exhibit similar trends in the vertical direction (Figure 10), gradually decreasing from bottom to top. The highest contents and enrichment factors of Mo and U are observed in TST1+HST1: Mo = 0.65–46.70 ppm (average 22.00 ppm), U = 4.94–16.30 ppm (average 9.90 ppm), Mo<sub>EF</sub> = 0.97–105.05 (average 46.92), U<sub>EF</sub> = 2.34–11.72 (average 6.37). The content and enrichment factors of Mo and U in TST2 exhibit a significant decrease: Mo = 0.92–15.7 ppm (average 2.62 ppm), U = 2.54–12.10 ppm (average 4.76 ppm), Mo<sub>EF</sub> = 0.73–35.85 (average 4.75), U<sub>EF</sub> = 1.61–8.78 (average 2.74). The lowest contents and enrichment factors of Mo and U are found in HST2: Mo = 0.10–1.96 ppm (average 0.43 ppm), U = 1.12–3.30 ppm (average 2.84 ppm), Mo<sub>EF</sub> = 0.19–3.27 (average 0.76), U<sub>EF</sub> = 0.97–1.90 (average 1.62).

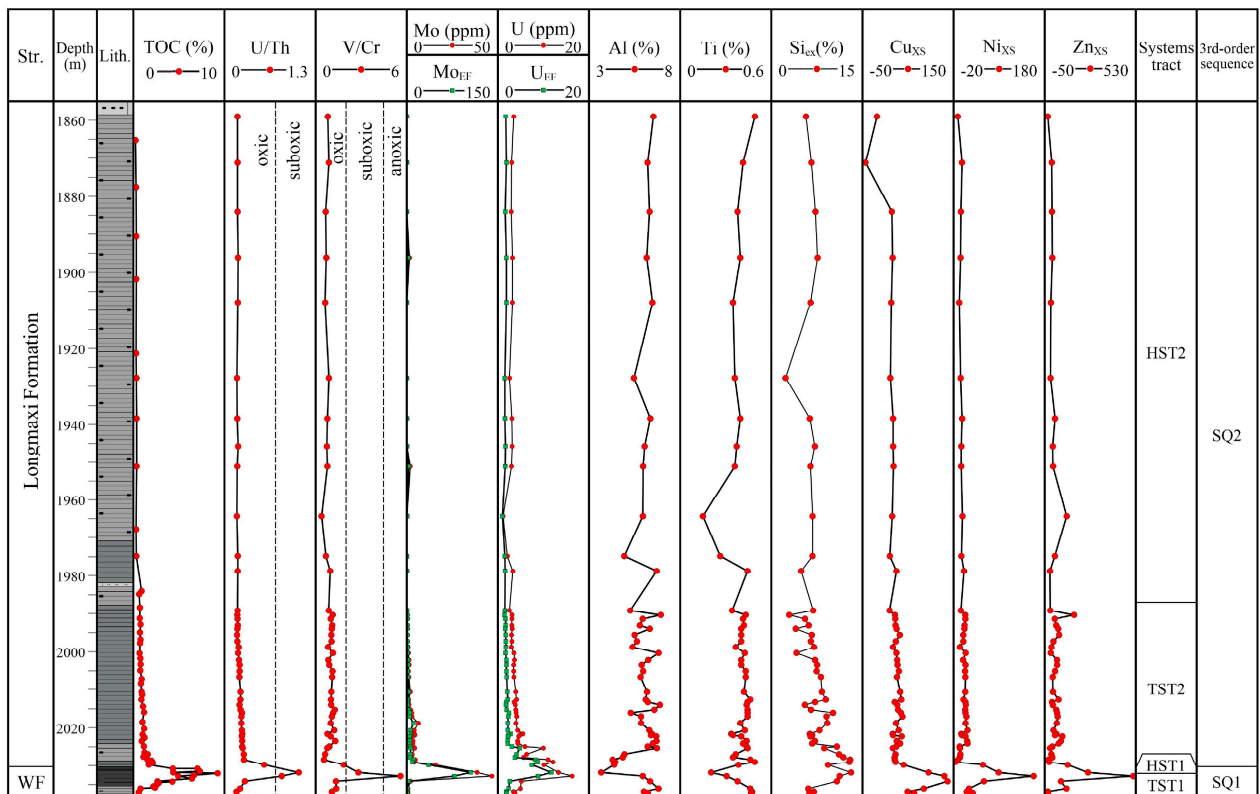


**Figure 10.** Vertical variation of U/Th, V/Cr, Mo–U, Mo<sub>EF</sub>, U<sub>EF</sub>, Al, Ti, Si<sub>ex</sub>, Cu<sub>XS</sub>, Ni<sub>XS</sub>, and Zn<sub>XS</sub> in the Wufeng–Longmaxi Formation shale samples from well YC1. Str. = Stratigraphy, WF = Wufeng Formation, Lith. = Lithology, TST = Transgressive systems tract, HST = Highstand systems tract.

The vertical trends of Cu<sub>XS</sub>, Ni<sub>XS</sub>, and Zn<sub>XS</sub> changes are generally similar (Figure 10), gradually decreasing from bottom to top. The values of Cu<sub>XS</sub>, Ni<sub>XS</sub>, and Zn<sub>XS</sub> in TST1+HST1 are the highest, with averages of 93.09 ppm, 54.24 ppm, and 136.61 ppm, respectively. In TST2, these values are significantly lower, averaging 25.58 ppm, 3.16 ppm, and 19.45 ppm, respectively. HST2 exhibits the lowest values for Cu<sub>XS</sub>, Ni<sub>XS</sub>, and Zn<sub>XS</sub>, with averages of 7.99 ppm, −3.48 ppm, and 3.51 ppm, respectively.

Similarly, the Si<sub>ex</sub> content also gradually decreases from bottom to top (Figure 10). The highest Si<sub>ex</sub> content is observed in TST1+HST1, with an average of 8.36%. TST2 shows a significant decrease, averaging 7.77%, while HST2 has the lowest Si<sub>ex</sub> content, averaging 6.20%.

## 5. Discussion

### 5.1. Influence of the Depositional Environment on Organic Matter Accumulation and Mineralogical Composition

#### 5.1.1. Influence of the Depositional Environment on Organic Matter Accumulation

Through the assessment of U/Th, V/Cr,  $Mo_{EF}$ , and  $U_{EF}$ , it can be inferred that the deposition of TST1 and HST1 intervals took place under suboxic conditions, whereas the deposition of TST2 and HST2 intervals occurred under oxic conditions (Figure 10). Additionally, the Mo and U contents in the HST2 interval are lower compared to those in the TST2 interval, approaching levels identified in PAAS shale. This implies a greater degree of bottom water oxidation during HST2 deposition than during TST2. By evaluating  $Cu_{XS}$ ,  $Ni_{XS}$ , and  $Zn_{XS}$ , it is possible to infer that paleoproductivity during the TST1 and HST1 periods was relatively high, medium during the TST2 period, and relatively low during the HST2 period.  $Mo_{EF}$ ,  $U_{EF}$ , U/Th, V/Cr,  $Cu_{XS}$ ,  $Ni_{XS}$ , and  $Zn_{XS}$  exhibit the same vertical change trend as TOC (Figure 10), indicating a strong positive correlation between these factors and TOC. This suggests that the enrichment of OM is influenced by both paleoproductivity and paleoredox conditions. Previous studies have demonstrated that OM accumulation is governed by production and preservation, and high paleoproductivity and anoxic conditions can enhance OM accumulation [73].

During the Kaidi period, global sea levels rose due to the influence of the Boda global warming event. Subsequently, global cooling and the impact of the Hirnantian glaciation caused a gradual fall in sea levels. As a result, the TST1 and HST1 intervals in the study area were deposited at the margin of the deep-water continental shelf (Figure 11A), under anoxic bottom water conditions and high paleoproductivity. The high paleoproductivity during the TST1 and HST1 intervals implies substantial nutrient input, promoting the proliferation of algae and, consequently, the transport of a substantial amount of OM to the seafloor sediments. Furthermore, the suboxic bottom water conditions prevailing during the deposition of the TST1 and HST1 intervals facilitated the preservation of OM, leading to the formation of OM-rich intervals. Following the Hirnantian, global warming and glacier melting caused a rapid rise in global sea levels. However, regional tectonic uplift, induced by the Kwangsian Orogeny during the Late Ordovician–Early Silurian, led to a decline in the regional sea level [74]. Consequently, the TST2 interval in the study area was deposited on a shallow continental shelf (Figure 11B). This shift resulted in reduced ancient productivity within sedimentary areas and a decrease in nutrient availability in water bodies, hindering the proliferation of algae. Additionally, the prevalence of oxic bottom water conditions during the deposition of the TST2 interval did not favor OM preservation, resulting in a notable reduction in TOC during this interval. During the Aeronian period, continuous regional tectonic uplift further lowered the regional sea level [74]. Consequently, the HST2 interval in the study area was deposited on a shallow continental shelf (Figure 11C). In comparison to the TST2 interval, during the sedimentation of the HST2 interval, the paleoproductivity further declined, and bottom water oxidation was more pronounced, leading to minimal OM enrichment during this period.

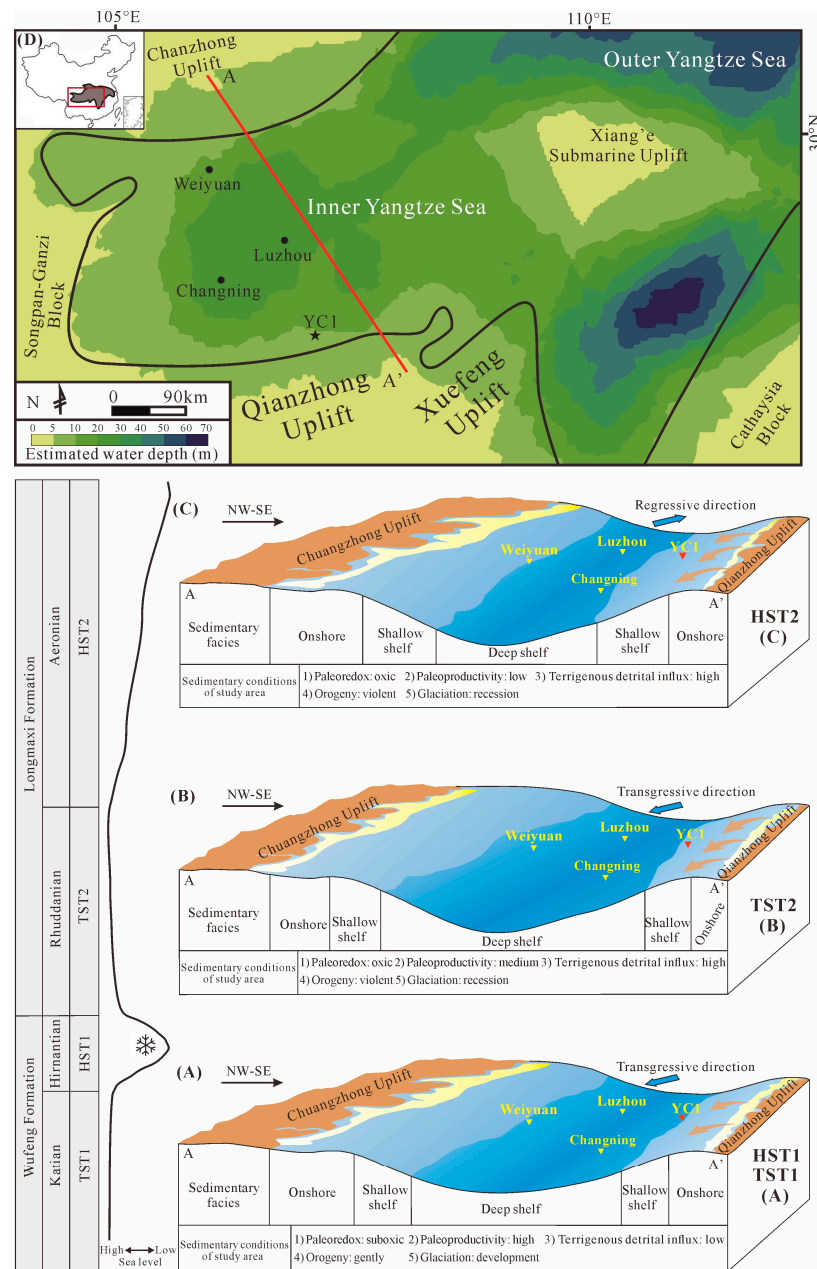


**Figure 11.** (A–C) The sequence stratigraphic evolution model of the Wufeng–Longmaxi Formation in the study area (modified from [75]). (D) Palaeogeographic map during the Mid-Hirnantian period (modified from [76]).

### 5.1.2. Influence of the Depositional Environment on Mineralogical Composition

XRD analysis reveals that the predominant minerals in the Wufeng–Longmaxi Formation shale are quartz, carbonate minerals, and clay minerals. The minerals present in the shale are mainly terrigenous and authigenic [77]. Al and Ti serve as reliable indicators reflecting terrigenous detrital influx [55], with Al mainly originating from fine-grained aluminosilicate clay minerals [40], while Ti is typically associated with clay and heavy minerals [78]. The contents of Al and Ti in the Wufeng–Longmaxi Formation shale in the study area exhibit a strong correlation and mirror the distribution of clay mineral content (Figure 12A). In comparison to TST1 and HST1, the Al and Ti contents in TST2 and HST2 shales show a significant increase (Figure 10), suggesting a higher terrigenous detrital influx during the deposition process. Consequently, the elevated content of clay minerals in TST2 and HST2 shales can be attributed to this increased terrigenous detrital influx.

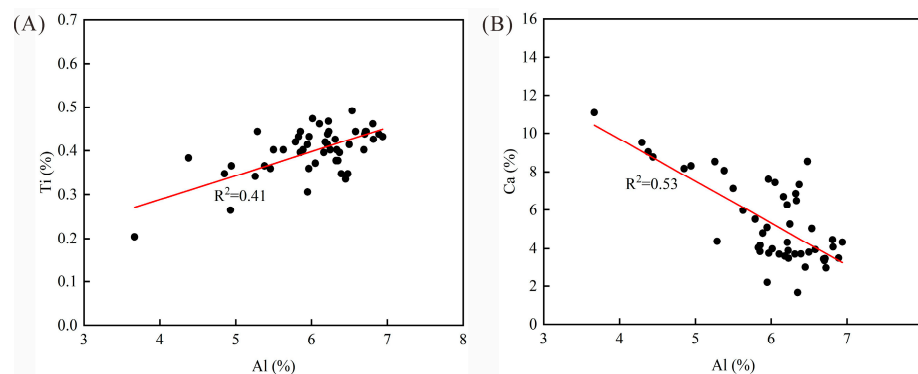


**Figure 12.** (A) Relationship between Al and Ti for the shale samples from the Wufeng–Longmaxi Formation. (B) Relationship between Al and Ca for the shale samples from the Wufeng–Longmaxi Formation.

According to the shape, size, and CL intensity of quartz, the type of quartz can be determined. Previous studies have demonstrated that the CL intensity of terrigenous quartz is stronger than that of authigenic quartz [79,80]. SEM observations indicate that the quartz particles in TST1 and HST1 shales are mostly small, appearing as aggregates and symbiotic with OM, with weak CL intensity (Figure 13A,B). This suggests that the quartz in this shale section is primarily authigenic. On the other hand, the quartz particles in TST2 and HST2 shales are mostly large and irregular in shape, exhibiting strong CL intensity (Figure 13C,D). These observations indicate that the majority of quartz in this interval is terrigenous quartz. Furthermore, the calculation results reveal that the average  $Si_{ex}$  content of TST1 and HST1 shales is the highest, indicating a high content of authigenic quartz in this section. In comparison, the average  $Si_{ex}$  content in TST2 and HST2 shale samples decreased, suggesting a reduction in the content of authigenic quartz when compared to TST1 and HST1.

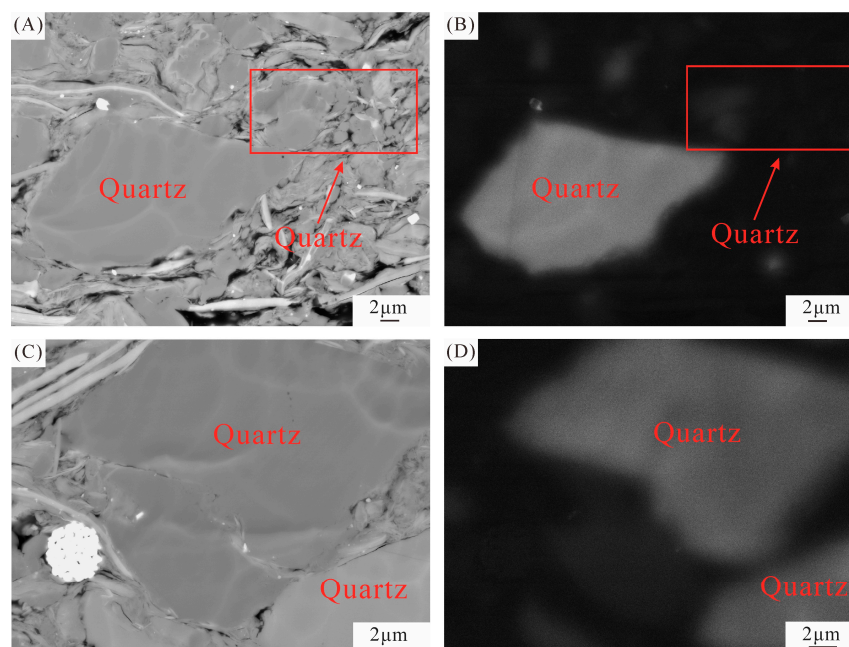


**Figure 13.** SEM and SEM-CL images of quartz in the Wufeng–Longmaxi Formation shale samples. (A) SEM image showing a single large quartz grain and its surrounding smaller quartz grains, TST1. (B) SEM-CL image of picture A showing strong luminescence of the large quartz grain and weak luminescence of the smaller quartz grains, TST1. (C) SEM image of two large quartz grains, TST2. (D) SEM-CL image of picture C showing two large quartz grains with strong luminescence, TST2.

Previous studies have shown that authigenic quartz in shale can originate from various processes, such as the dissolution and reprecipitation of siliceous biological skeletons, the conversion of clay minerals, the pressure dissolution of clastic quartz, hydrothermal input of silicon, and alteration of volcanic glass debris [34,80]. In the Wufeng–Longmaxi Formation shale, terrigenous quartz is primarily present as isolated particles within the shale matrix rather than in grain-to-grain contacts (Figure 13C,D). This observation indicates that the pressure dissolution of terrigenous quartz is not the primary source of authigenic quartz. To recognize the hydrothermal origin of silica, Al–Fe–Mn plots are commonly utilized [81]. In the case of the Wufeng–Longmaxi Formation samples, all of them plot in the non-hydrothermal area (Figure 14A), suggesting that hydrothermal silicon is not the main source of authigenic quartz. Quartz formed through the conversion of clay minerals (illite sericitization, muscovite illiteization, kaolinite illiteization, and chloritization) is typically observed as sheet-like quartz cement or secondarily enlarged edges of terrigenous quartz [63,82–84]. Moreover, the strong negative correlation between  $Si_{ex}$  and Al (Figure 14B) suggests that authigenic quartz is not primarily derived from the conversion of clay minerals. Additionally, the Rb/ $K_2O$  ratio can be used to assess the degree of silica from volcanic ash alteration in the sample [85]. A low Rb/ $K_2O$  ratio indicates the presence of a significant amount of silica provided by volcanic ash alteration [86,87]. The Rb/ $K_2O$  ratio of shale samples from the Wufeng–Longmaxi Formation is similar to that of PAAS shale, implying that the alteration of volcanic glass debris is not the main source of silicon (Figure 14C).

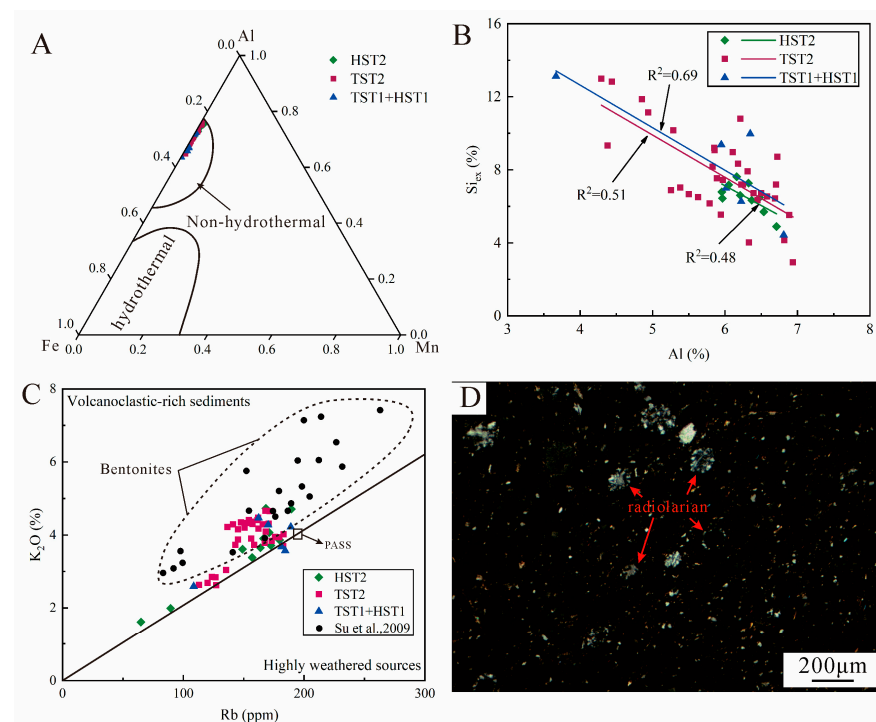


**Figure 14.** Silicon source discrimination diagrams. (A) Al–Fe–Mn ternary plot. (B) Relationship between Al and  $Si_{ex}$ . (C) Relationship between  $K_2O$  and Rb ( $K_2O$  and Rb concentrations of bentonites are from [87]). (D) Radiolarians in the shale samples from the Wufeng–Longmaxi Formation.

Based on the preceding discussion, the  $Si_{ex}$  in shale samples appears to be primarily of biogenic origin. The enrichment of biogenic silicon often corresponds well to conditions of sedimentary water with high paleoproductivity [88]. Among the shales, TST1 and HST1 exhibit the highest average  $Si_{ex}$  content, indicating deposition in a water environment with high paleoproductivity, fostering prolific reproduction of siliceous organisms. Additionally, a significant number of siliceous radiolarian fossils were observed in the thin sections of TST1 and HST1 shale samples (Figure 14D). The breakdown of siliceous organisms can

contribute to a rich supply of silica for the precipitation of authigenic quartz during early diagenesis [82].

Generally speaking, Ca mainly originates from carbonate minerals [55]. A strong negative correlation between Ca and Al is evident (Figure 12B), indicating that the carbonate minerals in the shale of Wufeng–Longmaxi Formation in the study area are predominantly authigenic. Recent research has demonstrated that within the sulfate and methane bacterial reduction zone, bacteria increase the concentration of bicarbonate ions in sedimentary water through sulfate reduction (Equation (4)) and methanogenesis (Equation (5)). This process leads to the supersaturation of carbonate mineral composition in the sedimentary water, resulting in precipitation and formation of carbonate minerals [89–91]. The deposition of TST1 and HST1 intervals occurred in a sedimentary environment with suboxic bottom waters and high paleoproductivity, facilitating the retention of sufficient OM to support bacterial sulfate reduction and methanogenesis. This process consumes  $\text{SO}_4^{2-}$ , increases the concentration of bicarbonate ions in the sedimentary water, promotes the combination of  $\text{Ca}^{2+}$  and  $\text{Mg}^{2+}$  with bicarbonate ions, and facilitates the formation of carbonate minerals. Consequently, the content of carbonate minerals in this section is notably high.



### 5.2. Relationship between Pore Types and Porosity

The porosity of shale samples was determined using the helium porosity method, with results showing that the porosity of TST1 and HST1 shale varies from 0.9% to 2.9% (average = 2.0%). In the case of TST2 shale, porosity ranges from 0.7 to 1.8% (average = 1.1%), while HST2 shale exhibits porosity in the range of 1.6 to 2.2% (average = 1.8%).

The correlation between TOC and porosity in TST1 and HST1 shale is notably stronger than the correlation between inorganic minerals (such as carbonates, quartz, and clay minerals) and porosity (Figure 15). This suggests that OM pores significantly contribute to the overall porosity, which aligns with the SEM observations (Figure 9). SEM observations of shale samples from this interval revealed the presence of abundant authigenic quartz grains of biogenic origin, formed during early diagenesis. These authigenic quartz grains are small in size, numerous, and interconnected, contributing to the formation of a supportive framework along terrigenous quartz. This framework exhibits resistance to compaction, thereby preserving a substantial number of primary interparticle pores (Figure 16A,B). However, these residual primary interparticle pores are frequently filled with resilient particles, including OM and clay minerals (Figure 16C), leading to fewer pores associated with quartz (Figure 9). Consequently, no significant correlation exists between quartz and porosity. Carbonate minerals, due to their chemically unstable nature, can be dissolved by the organic acids generated during OM pyrolysis, resulting in the creation of numerous dissolution pores (Figure 9). As a result, a positive correlation is observed between carbonate minerals and porosity (Figure 15B). The content of clay minerals in this interval is relatively low. Clay minerals often coexist with OM and are commonly observed filling primary interparticle pores, occupying a significant portion of the pore space. Although clay minerals occasionally develop interparticle pores, a majority of them are filled with OM (Figure 16D). Consequently, there is a negative correlation between clay minerals and porosity.

The correlation between TOC and carbonate minerals in TST2 shale shows a positive relationship with porosity, but this correlation is weaker compared to that of TST1 and HST1 shale (Figure 15). TST2 shale predominantly consists of scattered and striped OM, whereas TST1 and HST1 shale mainly contain gap-filling OM (Figure 6C). Statistics reveal that the areal porosity of scattered and striped OM is generally lower than that of gap-filling OM. Therefore, it is believed that the change in OM type is the primary reason for the attenuation of the correlation between TOC and porosity in TST2 shale. Due to the lower OM content in this interval, there is a reduction in the generation of organic acids during

OM pyrolysis, leading to a decrease in the formation of dissolution pores in carbonate minerals (Figure 9). Consequently, the correlation between carbonate minerals and porosity weakens. In comparison to the TST1 and HST1 intervals, the shale samples within this interval contain an increased amount of terrigenous detrital minerals, primarily clay minerals and terrigenous quartz. The interparticle pores within clay minerals contribute more significantly to porosity (Figure 9). Terrigenous quartz is often observed in isolated particle forms within the shale matrix and is surrounded by clay minerals, making a lesser contribution to porosity.

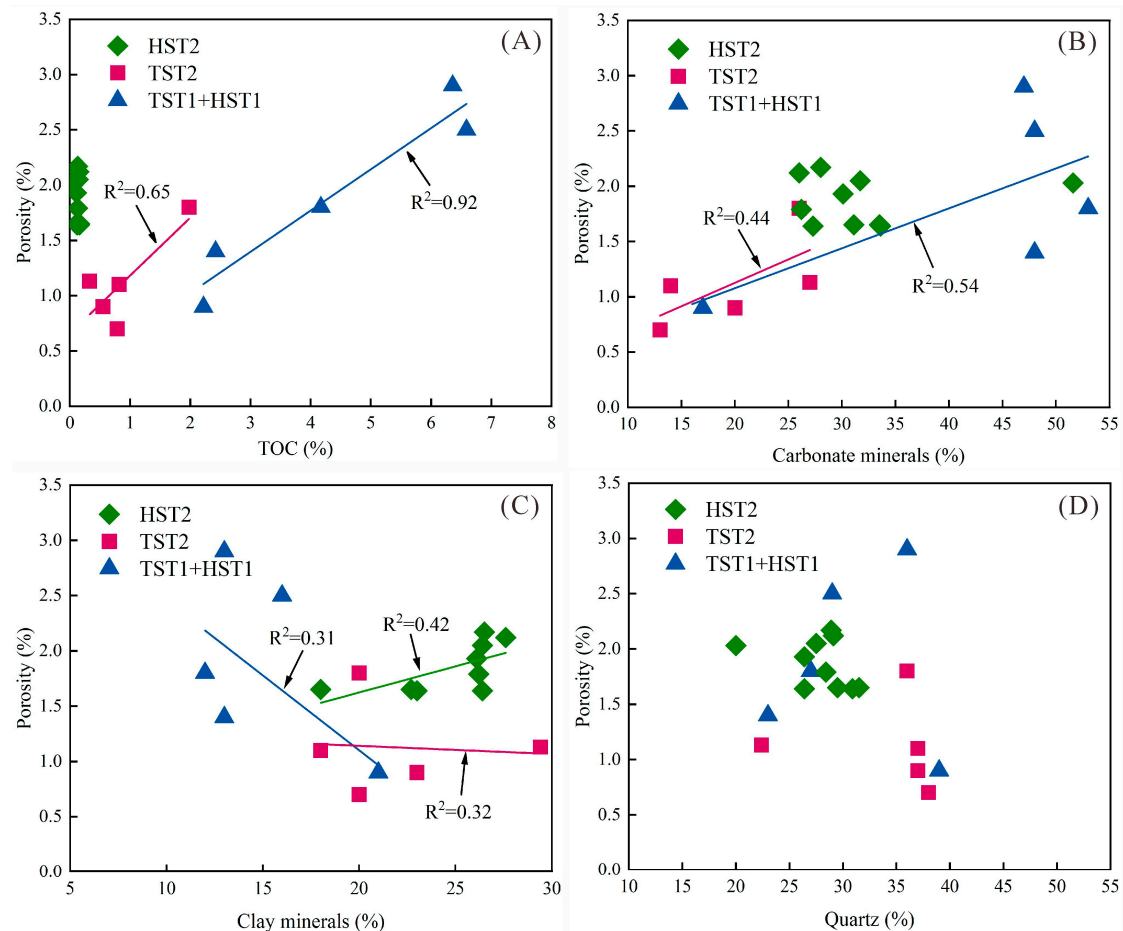


**Figure 15.** Relationship between TOC content, carbonate minerals, clay minerals, quartz, and porosity for the shale samples from the Wufeng–Longmaxi Formation. (A) Porosity vs. TOC content. (B) Porosity vs. carbonate minerals content. (C) Porosity vs. clay minerals content. (D) Porosity vs. quartz content.

The positive correlation between clay minerals and porosity in HST2 shale, in contrast to the lack of significant correlation between TOC, carbonates, and quartz with porosity, suggests that the interparticle pores within clay minerals play a substantial role in porosity development (Figure 15). The HST2 shale exhibits relatively low OM content, primarily derived from graptolites. Graptolites have limited hydrocarbon generation potential, resulting in underdeveloped OM pores. In comparison to the TST1 and HST1 intervals, the shale within this interval contains a higher concentration of clay minerals, and interparticle pores are frequently observed within clay aggregates (Figure 9). The content of brittle minerals is relatively low and mainly comprises terrigenous quartz and carbonate minerals. Terrigenous quartz is typically distributed sporadically within the shale matrix, surrounded by clay minerals, and rarely comes into contact with other terrigenous quartz. During early diagenesis, it is challenging to form a rigid framework, and primary pores tend to collapse

due to compaction. Consequently, quartz contributes less to porosity (Figure 9). Carbonate minerals are primarily cemented among terrigenous minerals, leading to a substantial reduction in primary pores. Additionally, the small quantity of OM is insufficient to generate a substantial amount of organic acid for dissolving carbonate minerals, resulting in a limited contribution of intraparticle pores in carbonate minerals to overall porosity.

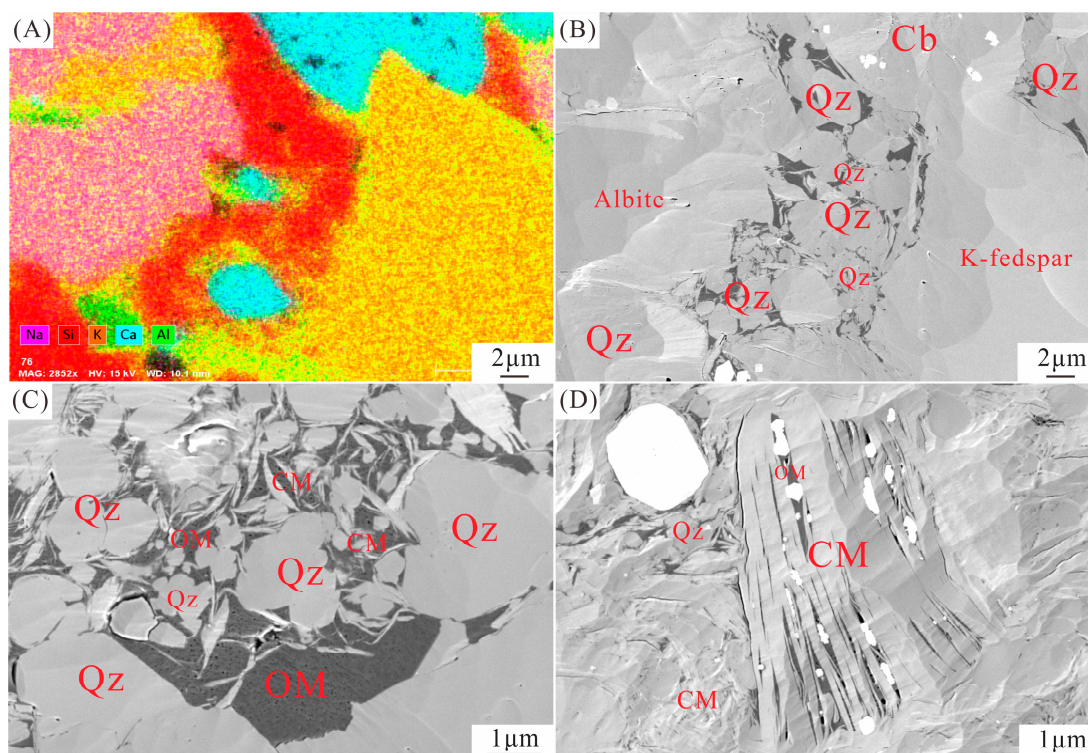


**Figure 16.** (A) EDS images of TST1 shale samples. (B) The SEM image in picture A demonstrates that the authigenic quartz is interconnected, forming a rigid framework that effectively resists compaction. (C) The pores between the authigenic quartz are filled with OM and clay minerals. (D) The pores between clay minerals are filled with OM. The mineral phases in the EDS image are quartz (red), albite (aubergine), carbonate (blue), K-feldspar (orange), and clay minerals (bright yellow). Qz, quartz; Cb, carbonate minerals; OM, organic matter; CM, clay minerals. (For interpretation of the references to color in this figure legend, the reader is referred to the Web version of this article.)

### 5.3. Formation and Evolution of Shale Pores in Different System Tracts

The OM content, types, mineral genesis, and composition in shale are collectively determined by their position within the sequence framework and distinct depositional environments. Therefore, the evolution of diagenesis has led to variations in the development of shale pore types in different sequences (Figure 17). During the deposition of TST1 and HST1 intervals, a period of high paleoproductivity promoted the proliferation of algae and siliceous organisms, favoring the enrichment of OM and authigenic quartz. In the early diagenesis phase, the rigid mineral framework formed by authigenic quartz was capable of withstanding compaction, thereby preserving a significant number of primary interparticle pores. In the middle and late stages of diagenesis, primary OM underwent thermal degradation and transformed into pyrobitumen. Subsequently, these pyrobitumens migrate short distances, filling primary interparticle pores and leading to the formation of gap-filling OM. During this phase, OM pores became widespread. Despite increasing compaction with burial depth, the integrity of gap-filling OM pores was maintained by a rigid network of authigenic quartz. As temperature and pressure increased, the transformation of clay minerals (e.g., from montmorillonite to mixed-layer clays such as illite) generated a limited number of interparticle pores. Due to the unstable chemical properties of carbonate

minerals, they were subject to corrosion by acidic fluids, including organic acids formed during hydrocarbon generation at various stages of diagenesis, resulting in the creation of numerous dissolution pores. Typically, these dissolution pores were preserved within or along the edges of carbonate minerals.

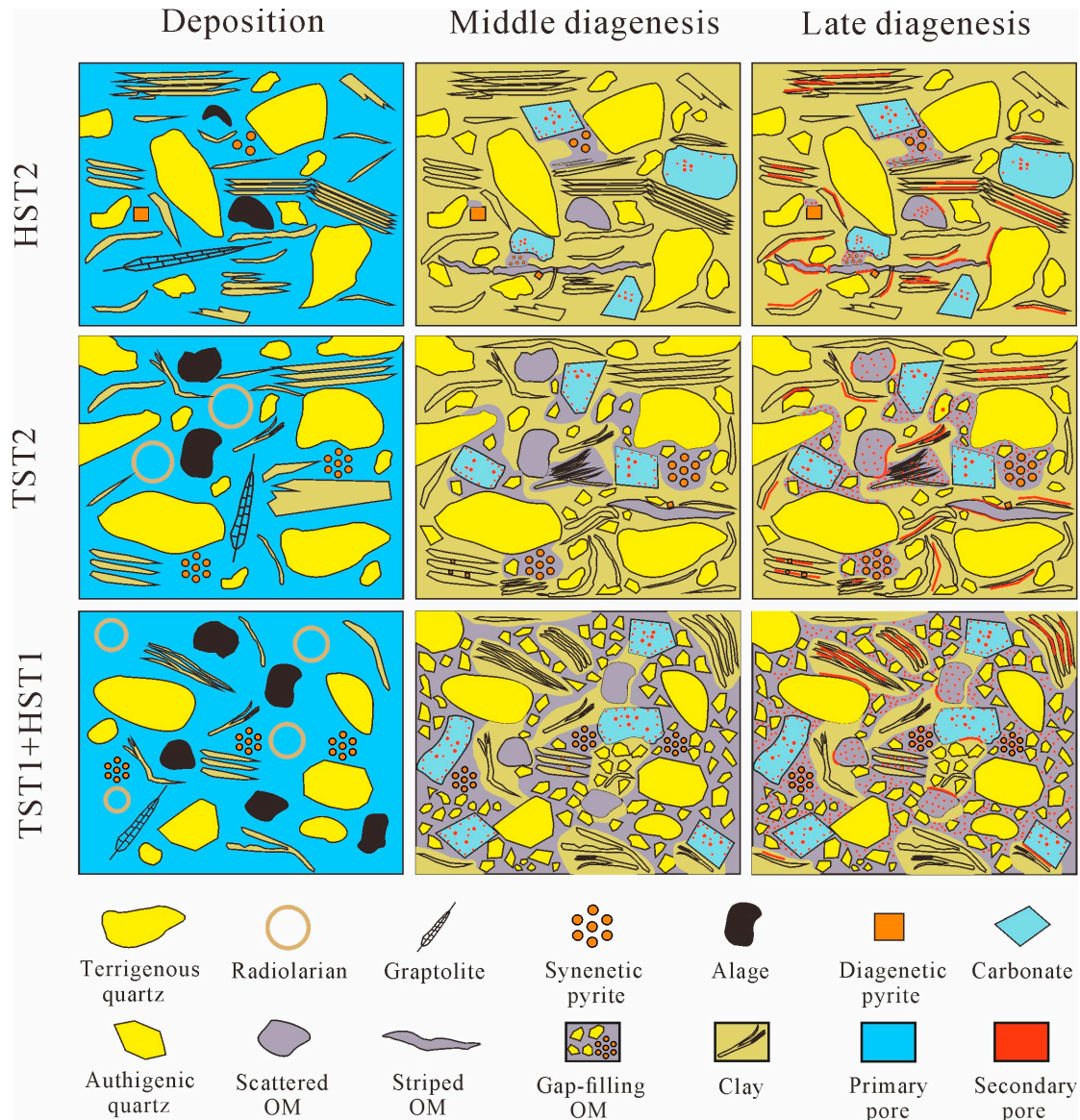


**Figure 17.** Evolutionary models of depositional and diagenetic processes in shale pores across different systems tracts.

During the TST2 sedimentary period, both paleoproductivity and bottom water reduction decreased significantly, leading to a reduction in OM abundance and authigenic quartz content. In comparison to TST1 and HST1 shale, TST2 shale exhibited decreased levels of OM pores and inorganic pores (interparticle pores and intraparticle pores).

During the HST2 sedimentary period, paleoproductivity and bottom water further decreased, resulting in almost no enrichment of OM. A significant influx of terrigenous detrital material led to the enrichment of clay minerals in this shale layer, and the OM was primarily composed of graptolites. During early diagenesis, a lack of protection from brittle minerals resulted in the compaction and closure of many primary pores. Graptolites had a chemical composition similar to that of type III kerogen, with limited hydrocarbon generation potential, which led to minimal development of OM pores during middle to late

diagenesis. During middle to late diagenesis, the transformation of clay minerals generated more interparticle pores.

In general, TST1 and HST1 are the sweet spots for shale gas exploration and development in the study area. The high TOC and abundant authigenic quartz in the TST1 and HST1 are the keys to the formation of the “sweet spot”. The authigenic quartz filling the interparticle pores supports the pore network, and the rich OM forms a large number of OM pores and methane during the gas window.

## 6. Conclusions

(1) The sequence stratigraphic framework of the Wufeng–Longmaxi Formation in the study area was established through wavelet analysis. Within the northern Guizhou region, the Wufeng–Longmaxi Formation is segmented into two third-order sequences (SQ1 and SQ2). The Wufeng Formation encompasses TST1 and HST1, constituting one third-order sequence. Meanwhile, the Longmaxi Formation is composed of TST2 and HST2, forming another third-order sequence.

(2) Data extraction on the number, size, and area of various pore types allowed a quantitative assessment of their relative contributions to pore space. Within TST1 and HST1 shale, OM pores emerged as the dominant pore type, constituting over 65% of the porosity. Similarly, TST2 shale exhibited dominance of OM pores, contributing to over 45% of the porosity, although with an average OM areal porosity of 7.3%, notably lower than that in TST1 and HST1, which recorded 12.7%. Conversely, HST2 displayed inorganic pores as the dominant pore type, primarily composed of interparticle pores associated with clay minerals, contributing to over 50% of the porosity, while OM pores remained relatively undeveloped.

(3) The development of pore types in shale is intricately influenced by factors such as OM content, type, and mineral composition, subject to the control of both sedimentary processes and diagenetic pathways. Global and regional geological events have caused changes in marine paleoproductivity, redox conditions, and terrigenous detrital influx during the deposition of the Wufeng–Longmaxi Formation in the study area, resulting in significant disparities in OM content, types, and initial mineral composition across different sequences. Subsequently, variations in diagenetic evolution have led to divergent patterns in the development of shale pore types within these sequences.

**Author Contributions:** X.W.: Conceptualization, Investigation, Methodology, Writing—original draft. Z.X.: Investigation, Writing—review and editing. Z.Y.: Investigation. S.Z.: Writing—review and editing. S.T.: Supervision, Funding acquisition. D.L.: Methodology. All authors have read and agreed to the published version of the manuscript.

**Funding:** The project was financially supported by the Key Project of National Natural Science Foundation of China (grant no. 42302203).

**Data Availability Statement:** The research data of this article can be obtained from the corresponding author “Zhaodong Xi” through reasonable requests.

**Acknowledgments:** Supported by the Liaoning Key Laboratory of Green Development of Mineral Resources.

**Conflicts of Interest:** The authors declare no conflict of interest.

## References

1. Sohail, G.M.; Yasin, Q.; Radewan, A.E.; Emad, M.Z. Estimating hardness and Young’s modulus of shale using drill cuttings: Implications for hydraulic fracturing in shale gas reservoir development. *Gas Sci. Eng.* **2023**, *118*, 205116. [[CrossRef](#)]
2. Malozyomov, B.V.; Martyushev, N.V.; Kukartsev, V.V.; Tynchenko, V.S.; Bukhtoyarov, V.V.; Wu, X.; Tyncheko, Y.A.; Kukartsev, V.A. Overview of Methods for Enhanced Oil Recovery from Conventional and Unconventional Reservoirs. *Energies* **2023**, *16*, 4907. [[CrossRef](#)]
3. Fishman, N.S.; Hackley, P.C.; Lowers, H.A.; Hill, R.J.; Egenhoff, S.O.; Eberl, D.D.; Blum, A.E. The nature of porosity in organic-rich mudstones of the Upper Jurassic Kimmeridge Clay Formation, North Sea, offshore United Kingdom. *Int. J. Coal Geol.* **2012**, *103*, 32–50. [[CrossRef](#)]

4. Milliken, K.L.; Rudnicki, M.; Awwiller, D.N.; Zhang, T. Organic matter-hosted pore system, Marcellus Formation (Devonian), Pennsylvania. *AAPG Bull.* **2013**, *97*, 177–200. [[CrossRef](#)]
5. Ko, L.T.; Loucks, R.G.; Zhang, T.; Ruppel, S.C.; Shao, D. Pore and pore network evolution of Upper Cretaceous Boquillas (Eagle Ford-equivalent) mudrocks: Results from gold tube pyrolysis experiments. *AAPG Bull.* **2016**, *100*, 1693–1722. [[CrossRef](#)]
6. Wang, P.F.; Jiang, Z.X.; Ji, W.M.; Zhang, C.; Yuan, Y.; Chen, L.; Yin, L.S. Heterogeneity of intergranular, intraparticle and organic pores in Longmaxi shale in Sichuan Basin, South China: Evidence from SEM digital images and fractal and multifractal geometries. *Mar. Pet. Geol.* **2016**, *72*, 122–138. [[CrossRef](#)]
7. Nie, H.; Sun, C.; Liu, G.; Du, W.; He, Z. Dissolution pore types of the Wufeng Formation and the Longmaxi Formation in the Sichuan Basin, south China: Implications for shale gas enrichment. *Mar. Pet. Geol.* **2019**, *101*, 243–251. [[CrossRef](#)]
8. Xiong, S.; Gao, Z.; Wei, W.; Wang, Y. Differential effects of pore structure of mineral and maceral components on the methane adsorption capacity evolution of the lower jurassic Da'anzhai member of the Ziliujing Formation lacustrine shale, Sichuan Basin, China. *Mar. Pet. Geol.* **2023**, *147*, 106017. [[CrossRef](#)]
9. Loucks, R.G.; Reed, R.M.; Ruppel, S.C.; Jarvie, D.M. Morphology, Genesis, and Distribution of Nanometer-Scale Pores in Siliceous Mudstones of the Mississippian Barnett Shale. *J. Sediment. Res.* **2009**, *79*, 848–861. [[CrossRef](#)]
10. Loucks, R.G.; Reed, R.M.; Ruppel, S.C.; Hammes, U. Spectrum of pore types and networks in mudrocks and a descriptive classification for matrix-related mudrock pores. *AAPG Bull.* **2012**, *96*, 1071–1098. [[CrossRef](#)]
11. Xi, Z.; Tang, S.; Zhang, S.; Sun, K. Pore Structure Characteristics of Marine-Continental Transitional Shale: A Case Study in the Qinshui Basin, China. *Energy Fuels* **2017**, *31*, 7854–7866. [[CrossRef](#)]
12. Li, Y.; Schieber, J.; Fan, T.; Wei, X. Pore characterization and shale facies analysis of the Ordovician-Silurian transition of northern Guizhou, South China: The controls of shale facies on pore distribution. *Mar. Pet. Geol.* **2018**, *92*, 697–718. [[CrossRef](#)]
13. Wang, Q.; Wang, T.; Liu, W.; Zhang, J.; Feng, Q.; Lu, H.; Peng, P. Relationships among composition, porosity and permeability of Longmaxi Shale reservoir in the Weiyuan Block, Sichuan Basin, China. *Mar. Pet. Geol.* **2019**, *102*, 33–47. [[CrossRef](#)]
14. Cao, T.; Xu, H.; Liu, G.; Deng, M.; Cao, Q.; Yu, Y. Factors influencing microstructure and porosity in shales of the Wufeng-Longmaxi formations in northwestern Guizhou, China. *J. Pet. Sci. Eng.* **2020**, *191*, 107181. [[CrossRef](#)]
15. Xi, Z.; Tang, S.; Lash, G.G.; Ye, Y.; Lin, D.; Zhang, B. Depositional controlling factors on pore distribution and structure in the lower Silurian Longmaxi shales: Insight from geochemistry and petrology. *Mar. Pet. Geol.* **2021**, *130*, 105114. [[CrossRef](#)]
16. Gao, P.; Xiao, X.M.; Hu, D.F.; Lash, G.G.; Liu, R.B.; Cai, Y.D.; Wang, Z.H.; Zhang, B.Y.; Yuan, T.; Liu, S.Y. Effect of silica diagenesis on porosity evolution of deep gas shale reservoir of the Lower Paleozoic Wufeng-Longmaxi formations, Sichuan Basin. *Mar. Pet. Geol.* **2022**, *145*, 105873. [[CrossRef](#)]
17. Liu, J.; Zhu, Y.M.; Shang, F.H.; Feng, G.J.; Liu, Y.; Gao, B.; Li, S.K.; Kuang, F.F. Pore System Diversity and Control Factors of High-Overmature Shale-Taking the Lujiaping and Longmaxi Formation Shales as an Example. *Energy Fuels* **2023**, *37*, 9047–9065. [[CrossRef](#)]
18. De Boer, J.H. *The Structure and Properties of Porous Materials*; Butterworth-Heinemann: London, UK, 1958.
19. Liu, J.; Li, P.; Sun, Z.; Lu, Z.; Du, Z.; Liang, H.; Lu, D. A new method for analysis of dual pore size distributions in shale using nitrogen adsorption measurements. *Fuel* **2017**, *210*, 446–454. [[CrossRef](#)]
20. Zhang, Q.; Liu, Y.; Wang, B.; Ruan, J.; Yan, N.; Chen, H.; Wang, Q.; Jia, G.; Wang, R.; Liu, H.; et al. Effects of pore-throat structures on the fluid mobility in chang 7 tight sandstone reservoirs of longdong area, Ordos Basin. *Mar. Pet. Geol.* **2022**, *135*, 105407. [[CrossRef](#)]
21. Chen, Q.; Zhang, J.; Tang, X.; Li, W.; Li, Z. Relationship between pore type and pore size of marine shale: An example from the Sinian-Cambrian formation, upper Yangtze region, South China. *Int. J. Coal Geol.* **2016**, *158*, 13–28. [[CrossRef](#)]
22. Liu, K.; Ostadhassan, M.; Gentzis, T.; Fowler, H. Image analysis of the pore structures: An intensive study for Middle Bakken. *J. Nat. Gas Sci. Eng.* **2019**, *61*, 32–45. [[CrossRef](#)]
23. Chandra, D.; Vishal, V.; Debarma, A.; Banerjee, S.; Pradhan, S.P.; Mishra, M.K. Role of Composition and Depth on Pore Attributes of Barakar Formation Gas Shales of Ib Valley, India, Using a Combination of Low-Pressure Sorption and Image Analysis. *Energy Fuels* **2020**, *34*, 8085–8098. [[CrossRef](#)]
24. Hui, S.; Pang, X.; Chen, Z.; Hu, T.; Shi, K.; Di, G.; Li, M.; Mei, S.; Li, M. Quantifying the relative contribution and evolution of pore types to shale reservoir space: Constraints from over-mature marine shale in the Sichuan Basin, SW China. *J. Asian Earth Sci.* **2023**, *249*, 105625. [[CrossRef](#)]
25. Chen, J.; Xiao, X. Evolution of nanoporosity in organic-rich shales during thermal maturation. *Fuel* **2014**, *129*, 173–181. [[CrossRef](#)]
26. Jiang, F.; Chen, D.; Chen, J.; Li, Q.; Liu, Y.; Shao, X.; Hu, T.; Dai, J. Fractal Analysis of Shale Pore Structure of Continental Gas Shale Reservoir in the Ordos Basin, NW China. *Energy Fuels* **2016**, *30*, 4676–4689. [[CrossRef](#)]
27. Teng, J.; Liu, B.; Mastalerz, M.; Schieber, J. Origin of organic matter and organic pores in the overmature Ordovician-Silurian Wufeng-Longmaxi Shale of the Sichuan Basin, China. *Int. J. Coal Geol.* **2022**, *253*, 103970. [[CrossRef](#)]
28. Zhang, W.T.; Hu, W.X.; Borjigin, T.; Zhu, F. Pore characteristics of different organic matter in black shale: A case study of the Wufeng-Longmaxi Formation in the Southeast Sichuan Basin, China. *Mar. Pet. Geol.* **2020**, *111*, 33–43. [[CrossRef](#)]
29. Hao, F.; Zou, H.; Lu, Y. Mechanisms of shale gas storage: Implications for shale gas exploration in China. *AAPG Bull.* **2013**, *97*, 1325–1346. [[CrossRef](#)]
30. Dai, J.; Zou, C.; Liao, S.; Dong, D.; Ni, Y.; Huang, J.; Wu, W.; Gong, D.; Huang, S.; Hu, G. Geochemistry of the extremely high thermal maturity Longmaxi shale gas, southern Sichuan Basin. *Org. Geochem.* **2014**, *74*, 3–12. [[CrossRef](#)]

31. Wu, J.G.; Yuan, Y.; Niu, S.Y.; Wei, X.F.; Yang, J.J. Multiscale characterization of pore structure and connectivity of Wufeng–Longmaxi shale in Sichuan Basin, China. *Mar. Pet. Geol.* **2020**, *120*, 104514. [[CrossRef](#)]
32. Knapp, L.J.; Ardakani, O.H.; Uchida, S.; Nanjo, T.; Otomo, C.; Hattori, T. The influence of rigid matrix minerals on organic porosity and pore size in shale reservoirs: Upper Devonian Duvernay Formation, Alberta, Canada. *Int. J. Coal Geol.* **2020**, *227*, 103525. [[CrossRef](#)]
33. Zhao, J.; Jin, Z.; Jin, Z.; Wen, X.; Geng, Y. Origin of authigenic quartz in organic-rich shales of the Wufeng and Longmaxi Formations in the Sichuan Basin, South China: Implications for pore evolution. *J. Nat. Gas Sci. Eng.* **2017**, *38*, 21–38. [[CrossRef](#)]
34. Xi, Z.; Tang, S.; Zhang, S.; Yi, Y.; Dang, F.; Ye, Y. Characterization of quartz in the Wufeng Formation in northwest Hunan Province, south China and its implications for reservoir quality. *J. Pet. Sci. Eng.* **2019**, *179*, 979–996. [[CrossRef](#)]
35. Xi, Z.; Tang, S.; Zhang, S.; Ye, Y. Factors Controlling Organic Matter Accumulation in the Wufeng–Longmaxi Formations in Northwestern Hunan Province: Insights from Major/Trace Elements and Shale Composition. *Energy Fuels* **2020**, *34*, 4139–4152. [[CrossRef](#)]
36. Dong, T.; He, S.; Chen, M.F.; Hou, Y.G.; Guo, X.W.; Wei, C.; Han, Y.J.; Yang, R. Quartz types and origins in the paleozoic Wufeng–Longmaxi Formations, Eastern Sichuan Basin, China: Implications for porosity preservation in shale reservoirs. *Mar. Pet. Geol.* **2019**, *106*, 62–73. [[CrossRef](#)]
37. Wang, Y.; Xu, S.; Hao, F.; Zhang, B.; Shu, Z.; Gou, Q.; Lu, Y.; Cong, F. Multiscale petrographic heterogeneity and their implications for the nanoporous system of the Wufeng–Longmaxi shales in Jiaoshiha area, Southeast China: Response to depositional–diagenetic process. *GSA Bull.* **2019**, *132*, 1704–1721. [[CrossRef](#)]
38. Phaye, D.K.; Bhattacharya, B.; Chakraborty, S. Heterogeneity characterization from sequence stratigraphic analysis of Paleocene–Early Eocene Cambay Shale formation in Jambusar–Broach area, Cambay Basin, India. *Mar. Pet. Geol.* **2021**, *128*, 104986. [[CrossRef](#)]
39. Crombez, V.; Baudin, F.; Rohais, S.; Riquier, L.; Euzen, T.; Pauthier, S.; Ducros, M.; Caron, B.; Vaisblat, N. Basin scale distribution of organic matter in marine fine-grained sedimentary rocks: Insight from sequence stratigraphy and multi-proxies analysis in the Montney and Doig Formations. *Mar. Pet. Geol.* **2017**, *83*, 382–401. [[CrossRef](#)]
40. Arthur, M.A.; Sageman, B.B. Marine black shales—Depositional mechanisms and environments of ancient-deposits. *Annu. Rev. Earth Planet. Sci.* **1994**, *22*, 499–551. [[CrossRef](#)]
41. Chen, L.; Lu, Y.; Jiang, S.; Li, J.; Guo, T.; Luo, C. Heterogeneity of the Lower Silurian Longmaxi marine shale in the southeast Sichuan Basin of China. *Mar. Pet. Geol.* **2015**, *65*, 232–246. [[CrossRef](#)]
42. Byun, U.H.; Lee, H.S.; Kwon, Y.K. Sequence stratigraphy in the middle Ordovician shale successions, mid-east Korea: Stratigraphic variations and preservation potential of organic matter within a sequence stratigraphic framework. *J. Asian Earth Sci.* **2018**, *152*, 116–131. [[CrossRef](#)]
43. Dong, T.; Harris, N.B.; Ayranci, K. Relative sea-level cycles and organic matter accumulation in shales of the Middle and Upper Devonian Horn River Group, northeastern British Columbia, Canada: Insights into sediment flux, redox conditions, and bioproductivity. *Geol. Soc. Am. Bull.* **2018**, *130*, 859–880. [[CrossRef](#)]
44. Kunzmann, M.; Schmid, S.; Blaikie, T.N.; Halverson, G.P. Facies analysis, sequence stratigraphy, and carbon isotope chemostratigraphy of a classic Zn–Pb host succession: The Proterozoic middle McArthur Group, McArthur Basin, Australia. *Ore Geol. Rev.* **2019**, *106*, 150–175. [[CrossRef](#)]
45. Liu, B.; Schieber, J.; Mastalerz, M.; Teng, J. Organic matter content and type variation in the sequence stratigraphic context of the Upper Devonian New Albany Shale, Illinois Basin. *Sediment. Geol.* **2019**, *383*, 101–120. [[CrossRef](#)]
46. Creaney, S.; Passey, Q.R. Recurring patterns of total organic carbon and source rock quality within a sequence stratigraphic framework. *AAPG Bull.* **1993**, *77*, 386–401.
47. Xu, C.; Rong, J.Y.; Yue, L.; Boucot, A.J. Facies patterns and geography of the Yangtze region, South China, through the Ordovician and Silurian transition. *Paleogeogr. Paleoclimatol. Paleocol.* **2004**, *204*, 353–372. [[CrossRef](#)]
48. Nie, H.; Zhang, B.; Liu, G.; Yan, C.; Li, D.; Lu, Z.; Zhang, G. Geological factors contributing to high shale gas yield in the Wufeng–Longmaxi Fms of Sichuan Basin: A case study of Well JY6-2HF in Fuling shale gas field. *Oil Gas Geol.* **2020**, *41*, 463–473.
49. Ma, Y.; Cai, X.; Zhao, P. China’s shale gas exploration and development: Understanding and practice. *Petroleum Explor. Dev.* **2018**, *45*, 589–603. [[CrossRef](#)]
50. Ye, Y.P.; Tang, S.H.; Xi, Z.D.; Jiang, D.X.; Duan, Y. Quartz types in the Wufeng–Longmaxi Formations in southern China: Implications for porosity evolution and shale brittleness. *Mar. Pet. Geol.* **2022**, *137*, 105479. [[CrossRef](#)]
51. Bosikov, I.I.I.; Martyushev, N.V.V.; Klyuev, R.V.V.; Tynchenko, V.S.S.; Kukartsev, V.A.A.; Ereemeeva, S.V.V.; Karlina, A.I.I. Complex Assessment of X-ray Diffraction in Crystals with Face-Centered Silicon Carbide Lattice. *Crystals* **2023**, *13*, 528. [[CrossRef](#)]
52. Li, J.; Tang, S.H.; Zhang, S.H.; Xi, Z.D.; Yang, N.; Yang, G.Q.; Li, L.; Li, Y.P. Paleo-environmental conditions of the Early Cambrian Niutitang Formation in the Fenggang area, the southwestern margin of the Yangtze Platform, southern China: Evidence from major elements, trace elements and other proxies. *J. Asian Earth Sci.* **2018**, *159*, 81–97. [[CrossRef](#)]
53. Xi, Z.D.; Tang, S.H.; Lash, G.G.; Zhang, B.; Lin, D.L. Geochemical characteristics of organic carbon and pyrite sulfur in Ordovician–Silurian transition shales in the Yangtze Platform, South China: Implications for the depositional environment. *Paleogeogr. Paleoclimatol. Paleocol.* **2021**, *563*, 110173. [[CrossRef](#)]

54. Sun, W.; Zuo, Y.; Wu, Z.; Liu, H.; Xi, S.; Shui, Y.; Wang, J.; Liu, R.; Lin, J. Fractal analysis of pores and the pore structure of the Lower Cambrian Niutitang shale in northern Guizhou province: Investigations using NMR, SEM and image analyses. *Mar. Pet. Geol.* **2019**, *99*, 416–428. [[CrossRef](#)]
55. Tribouvillard, N.; Algeo, T.J.; Lyons, T.; Riboulleau, A. Trace metals as paleoredox and paleoproductivity proxies: An update. *Chem. Geol.* **2006**, *232*, 12–32. [[CrossRef](#)]
56. Neubert, N.; Nagler, T.F.; Bottcher, M.E. Sulfidity controls molybdenum isotope fractionation into euxinic sediments: Evidence from the modern Black Sea. *Geology* **2008**, *36*, 775–778. [[CrossRef](#)]
57. McLennan, S.M. Relationships between the trace element composition of sedimentary rocks and upper continental crust. *Geochem. Geophys. Geosyst.* **2001**, *2*. [[CrossRef](#)]
58. Scott, C.; Lyons, T.W. Contrasting molybdenum cycling and isotopic properties in euxinic versus non-euxinic sediments and sedimentary rocks: Refining the paleoproxies. *Chem. Geol.* **2012**, *324*, 19–27. [[CrossRef](#)]
59. Algeo, T.J.; Maynard, J.B. Trace-element behavior and redox facies in core shales of Upper Pennsylvanian Kansas-type cyclothems. *Chem. Geol.* **2004**, *206*, 289–318. [[CrossRef](#)]
60. Brumsack, H.J. The trace metal content of recent organic carbon-rich sediments: Implications for Cretaceous black shale formation. *Paleogeogr. Paleoclimatol. Paleoecol.* **2006**, *232*, 344–361. [[CrossRef](#)]
61. Ross, D.; Bustin, R.M. Sediment geochemistry of the Lower Jurassic Gordondale Member, northeastern British Columbia. *Bull. Can. Pet. Geol.* **2006**, *54*, 337–365. [[CrossRef](#)]
62. Zhao, J.H.; Jin, Z.J.; Jin, Z.K.; Hu, Q.H.; Hu, Z.Q.; Du, W.; Yan, C.N.; Geng, Y.K. Mineral types and organic matters of the Ordovician-Silurian Wufeng and Longmaxi Shale in the Sichuan Basin, China: Implications for pore systems, diagenetic pathways, and reservoir quality in fine-grained sedimentary rocks. *Mar. Pet. Geol.* **2017**, *86*, 655–674. [[CrossRef](#)]
63. Niu, X.; Yan, D.T.; Zhuang, X.G.; Liu, Z.X.; Li, B.Q.; Wei, X.S.; Xu, H.W.; Li, D.W. Origin of quartz in the lower Cambrian Niutitang Formation in south Hubei Province, upper Yangtze platform. *Mar. Pet. Geol.* **2018**, *96*, 271–287. [[CrossRef](#)]
64. Yuan, X.; Guo, Y.; Yu, J.; Shen, Y.; Shao, Y. Correlation and analysis of well-log sequence with Milankovitch cycles as rulers: A case study of coal-bearing strata of late Permian in western Guizhou. *Int. J. Min. Sci. Technol.* **2013**, *23*, 563–568. [[CrossRef](#)]
65. Zhao, W.; Jiang, Z.; Qiu, L.; Chen, Y. Geological concept, method and application of sequence unit identification through wavelet analysis. *Oil Gas Geol.* **2010**, *31*, 436–441.
66. Yu, J.; Li, Z. Wavelet Transform of Logging Data and Its Geological Significance. *J. China Univ. Min. Technol.* **2003**, *32*, 336–339.
67. Deng, H. Discussion on problems of applying high resolution sequence stratigraphy. *J. Palaeogeogr.* **2009**, *11*, 471–480.
68. Zhao, Z.; Chen, X.; Pan, M.; Wu, X.; Zheng, X.; Pan, W. Milankovitch Cycles in the Upper Ordovician Lianglitage Formation in the Tazhong-Bachu Area, Tarim Basin. *Acta Geol. Sin.* **2010**, *84*, 518–536.
69. Yang, C.; Xiong, Y.; Zhang, J. A comprehensive re-understanding of the OM-hosted nanopores in the marine Wufeng-Longmaxi shale formation in South China by organic petrology, gas adsorption, and X-ray diffraction studies. *Int. J. Coal Geol.* **2020**, *218*, 103362. [[CrossRef](#)]
70. Delle Piane, C.; Ansari, H.; Li, Z.; Mata, J.; Rickard, W.; Pini, R.; Dewhurst, D.N.; Sherwood, N. Influence of organic matter type on porosity development in the Wufeng–Longmaxi Shale: A combined microscopy, neutron scattering and physisorption approach. *Int. J. Coal Geol.* **2022**, *249*, 103880. [[CrossRef](#)]
71. Li, X.; Jiang, Z.; Wang, P.; Song, Y.; Li, Z.; Tang, X.; Li, T.; Zhai, G.; Bao, S.; Xu, C.; et al. Porosity-preserving mechanisms of marine shale in Lower Cambrian of Sichuan Basin, South China. *J. Nat. Gas Sci. Eng.* **2018**, *55*, 191–205. [[CrossRef](#)]
72. Li, J.; Tang, S.; Zhang, S.; Li, L.; Wei, J.; Xi, Z.; Sun, K. Characterization of unconventional reservoirs and continuous accumulations of natural gas in the Carboniferous-Permian strata, mid-eastern Qinshui basin, China. *J. Nat. Gas Sci. Eng.* **2018**, *49*, 298–316. [[CrossRef](#)]
73. Lu, Y.B.; Jiang, S.; Lu, Y.C.; Xu, S.; Shu, Y.; Wang, Y.X. Productivity or preservation? The factors controlling the organic matter accumulation in the late Katian through Hirnantian Wufeng organic-rich shale, South China. *Mar. Pet. Geol.* **2019**, *109*, 22–35. [[CrossRef](#)]
74. Deng, X.; Yang, K.; Liu, Y.; She, Z. Characteristics and tectonic evolution of Qianzhong Uplift. *Earth Sci. Front.* **2010**, *17*, 79–89.
75. Huang, Z.; Li, Z.; Shi, W.; Yang, X.; Wang, X.; Young, S. Differential sedimentary mechanisms of Upper Ordovician-Lower Silurian shale in southern Sichuan Basin, China. *Mar. Pet. Geol.* **2023**, *148*, 106040. [[CrossRef](#)]
76. Li, N.; Li, C.; Fan, J.; Algeo, T.J.; Yan, D.; Zhu, G.; Wu, S.; Tang, S.; Cheng, M.; Jin, C. Sulfate-controlled marine euxinia in the semi-restricted inner Yangtze Sea (South China) during the Ordovician-Silurian transition. *Paleogeogr. Paleoclimatol. Paleoecol.* **2019**, *534*, 109281. [[CrossRef](#)]
77. Zhang, H.; Lin, B.; Bian, J.; Wu, J.; Yang, Q.; Yuan, L. Comparative study on organic-rich marine and continental shale: The case of Lower Paleozoic in south China and Carboniferous-Permian shale in North China. *Coal Geol. Explor.* **2018**, *46*, 88–95.
78. Li, Y.F.; Zhang, T.W.; Ellis, G.S.; Shao, D.Y. Depositional environment and organic matter accumulation of Upper Ordovician-Lower Silurian marine shale in the Upper Yangtze Platform, South China. *Paleogeogr. Paleoclimatol. Paleoecol.* **2017**, *466*, 252–264. [[CrossRef](#)]
79. Schieber, J.; Krinsley, D.; Riciputi, L. Diagenetic origin of quartz silt in mudstones and implications for silica cycling. *Nature* **2000**, *406*, 981–985. [[CrossRef](#)]
80. Milliken, K.L.; Ergene, S.M.; Ozkan, A. Quartz types, authigenic and detrital, in the Upper Cretaceous Eagle Ford Formation, South Texas, USA. *Sediment. Geol.* **2016**, *339*, 273–288. [[CrossRef](#)]

81. Adachi, M.; Yamamoto, K.; Sugisaki, R. Hydrothermal chert and associated siliceous rocks from the northern Pacific—Their geological significance as indication of ocean ridge activity. *Sediment. Geol.* **1986**, *47*, 125–148. [[CrossRef](#)]
82. Peltonen, C.; Marcussen, O.; Bjorlykke, K.; Jahren, J. Clay mineral diagenesis and quartz cementation in mudstones: The effects of smectite to illite reaction on rock properties. *Mar. Pet. Geol.* **2009**, *26*, 887–898. [[CrossRef](#)]
83. Thyberg, B.; Jahren, J. Quartz cementation in mudstones: Sheet-like quartz cement from clay mineral reactions during burial. *Petrol. Geosci.* **2011**, *17*, 53–63. [[CrossRef](#)]
84. Yang, X.R.; Yan, D.T.; Wei, X.S.; Zhang, L.W.; Zhang, B.; Xu, H.W.; Gong, Y.; He, J. Different formation mechanism of quartz in siliceous and argillaceous shales: A case study of Longmaxi Formation in South China. *Mar. Pet. Geol.* **2018**, *94*, 80–94.
85. Ran, B.; Liu, S.G.; Jansa, L.; Sun, W.; Yang, D.; Ye, Y.H.; Wang, S.Y.; Luo, C.; Zhang, X.; Zhang, C.J. Origin of the Upper Ordovician–lower Silurian cherts of the Yangtze block, South China, and their palaeogeographic significance. *J. Asian Earth Sci.* **2015**, *108*, 1–17. [[CrossRef](#)]
86. McLennan, S.M.; Taylor, S.R.; McCulloch, M.T.; Maynard, J.B. Geochemical and Nd–Sr isotopic composition of deep-sea turbidites: Crustal evolution and plate tectonic associations. *Geochim. Cosmochim. Acta* **1990**, *54*, 2015–2050. [[CrossRef](#)]
87. Su, W.; Huff, W.D.; Ettensohn, F.R.; Liu, X.; Zhang, J.; Li, Z. K-bentonite, black-shale and flysch successions at the Ordovician–Silurian transition, South China: Possible sedimentary responses to the accretion of Cathaysia to the Yangtze Block and its implications for the evolution of Gondwana. *Gondwana Res.* **2009**, *15*, 111–130. [[CrossRef](#)]
88. Ragueneau, O.; Treguer, P.; Leynaert, A.; Anderson, R.F.; Brzezinski, M.A.; Demaster, D.J.; Dugdale, R.C.; Dymond, J.; Fischer, G.; Francois, R.; et al. A review of the Si cycle in the modern ocean: Recent progress and missing gaps in the application of biogenic opal as a paleoproductivity proxy. *Glob. Planet. Chang.* **2000**, *26*, 317–365. [[CrossRef](#)]
89. Mazzullo, S.J. Organogenic dolomitization in peritidal to deep-sea sediments. *J. Sediment. Res.* **2000**, *70*, 10–23. [[CrossRef](#)]
90. Chukwuma, K.; Tsikos, H.; Wagner, N. Control of variability of primary grain assemblages on the stratigraphic differences in diagenetic processes and products in organic-rich sediments. *Sediment. Geol.* **2021**, *422*, 105966. [[CrossRef](#)]
91. Macquaker, J.; Taylor, K.G.; Keller, M.; Polya, D. Compositional controls on early diagenetic pathways in fine-grained sedimentary rocks: Implications for predicting unconventional reservoir attributes of mudstones. *AAPG Bull.* **2014**, *98*, 587–603. [[CrossRef](#)]

**Disclaimer/Publisher’s Note:** The statements, opinions and data contained in all publications are solely those of the individual author(s) and contributor(s) and not of MDPI and/or the editor(s). MDPI and/or the editor(s) disclaim responsibility for any injury to people or property resulting from any ideas, methods, instructions or products referred to in the content.